creative commons
COMMONS DEED

저작자표시-비영리-변경금지 2.0 대한민국

이용자는 아래의 조건을 따르는 경우에 한하여 자유롭게

- 이 저작물을 복제, 배포, 전송, 전시, 공연 및 방송할 수 있습니다.

다음과 같은 조건을 따라야 합니다:

저작자표시. 귀하는 원저작자를 표시하여야 합니다.

비영리. 귀하는 이 저작물을 영리 목적으로 이용할 수 없습니다.

변경금지. 귀하는 이 저작물을 개작, 변형 또는 가공할 수 없습니다.

- 귀하는, 이 저작물의 재이용이나 배포의 경우, 이 저작물에 적용된 이용허락조건을 명확하게 나타내어야 합니다.
- 저작권자로부터 별도의 허가를 받으면 이러한 조건들은 적용되지 않습니다.

저작권법에 따른 이용자의 권리는 위의 내용에 의하여 영향을 받지 않습니다.

이것은 이용허락규약(Legal Code)을 이해하기 쉽게 요약한 것입니다.

Disclaimer

dCollection

이학박사 학위논문

A Three-Type classification of Sudden Stratospheric Warming

성층권 돌연승온의 세 가지 유형 분류

2020년 2월

서울대학교 대학원

지구환경과학부

최혜선

Abstract

A Three-Type classification of Sudden Stratospheric Warming

Hyesun Choi

School of Earth and Environmental Sciences

Seoul National University

In existing literature, sudden stratospheric warming (SSW) events have been typically defined as displacement or split types. Detailed reexamination of SSW evolution has revealed that an SSW event often alters its type before and after the central day of the warming event. On the basis of this observation, we objectively define three types of SSW using wave amplitude: displacement–displacement (DD) type, displacement–split (DS) type, and split–split (SS) type. The geopotential height (GPH) amplitude of zonal wavenumbers 1 and 2 averaged over 55º–65ºN at 10 hPa was used as a criterion for the classification. If the amplitude of zonal wavenumber 1 is larger (smaller) than that of wavenumber 2 before and after the central day of SSW, the event is regarded as a DD (SS) type. If the amplitude of zonal wavenumber 1 is larger than that of wavenumber 2 before the central day but is smaller after that day, the event is regarded as a DS type. The above classification algorithm has been applied to both reanalysis data and model results.

We observe that conventional split-type SSW events identified by previous studies can be categorized as either DS- or SS type events, each type of which exhibits different evolution characteristics. In particular, they are distinctively different during the prewarming period. In the SS type, the characteristics of the conventional split type are more obvious, and the features that differ from those of the DD type are the most robust. The model results generally resemble the reanalysis data, particularly in the DD cases. Here, we also show that existence of a type-transition during the course of the SSW life cycle can be attributable to the condition of North Atlantic Oscillation (NAO) preceding before onset: Positive NAO favors SSW of DD type with no transition while negative NAO favors the DS type. We show that, in positive NAO precondition, vertical flux of wave activity immediately before onset is mostly contributed only by wavenumber 1 component, which contrasts with the relatively stronger contribution of wavenumber 2 in negative NAO pre-condition. Whole Atmosphere Community Climate Model (WACCM) simulation results are also consistent with the observational findings. Therefore, NAO can be regarded as a useful precursor for determining the type of forthcoming SSW events.

Keywords : sudden stratospheric warming, classification algorithm, displacement–displacement (DD) type, displacement–split (DS) type, and split–split (SS) type, North Atlantic Oscillation, precursor

Student Number : 2006-30124

Table of Contents

Abstract…….. i

List of Figures and Tables……...iv

1. Motivation and objectives……1

2. Data and model…….. 6

2.1 Data…… 6

2.2 Model…….7

3. Type Classification of SSW based on pre- and postwarming periods

…….. 10

3.1 Classification of SSW type……..……10

3.1.1 Classification algorithm……..……10

3.1.2 Objective definition of the displacement-split type……..14

3.1.3 Comparisons with other studies……...23

3.1.4 Characteristic features of the three SSW types……..29

3.2 Model results……...…43

4. Dependence of SSW type-transition on preceding NAO conditions

…….. 52

5. Summary and discussion……72

References…….....76

국문초록……...…84

List of Figures and Tables

Figure 1. Temporal evolution of the amplitude ratio of wave 2 to wave 1. Thin lines represent individual SSW events, and the thick line shows their composite mean. Ratios larger than 1.0 are shown with a red asterisk. (a) 13 wave-1-type SSW events; (b) 12 wave-2-type SSW events. The dashed line in (b) corresponds to an SSW event occurring on 24 January 2009 with maximum ratios of 14.9 on day –8 and 8.3 on day +11. It should be noted that the range of the vertical axis is different.

Figure 2. Same as Fig. 1 but for (a) seven DS types and (b) five SS types. The dashed line and the green line in (b) correspond to SSW events occurring on 24 January 2009 and on 24 February 2007, respectively. DS and SS types are defined in the manuscript.

Figure 3. Zonal perturbation GPH at 10 hPa with a five-day interval based on MERRA data. (a) DD-type warming on 22 February 2008; (b) DS-type warming on 8 December 1987; (c) SS-type warming on 1 January 1985. The contour interval is 200 m.

Figure 4. Temporal evolution of amplitude of waves 1 (black) and 2 (red) for the SS-type SSW in 1985 (Fig. 3c) from day -20 to day 20.

Figure 5. Differences in zonal mean zonal wind anomalies averaged from days -20 to -5 between DD and SS types for (a) 1958–2002 based on NCEP–NCAR data, (b) 1979–2014 based on NCEP–NCAR data, and (c) 1979–2014 based on MERRA data. The numbers of DD- and SS-type events are (a) 16 and 5, (b) 11 and 5, and (c) 13

and 5. The contour interval is 1.0 m s^{-1}. The blue and red contours indicate negative and positive differences, respectively. Gray shading indicates the region of statistical significance at the 90% confidence level.

Figure 6. Same as Fig. 5 but for differences between DD and DS+SS types. The numbers of DD- and DS+SS-type events are (a) 16 and 12 and (b) 11 and 11, respectively.

Figure 7. PCH anomaly based on the MERRA GPH anomaly averaged over 65°N–90°N for (a) 13 DD events, (b) 7 DS events, and (c) 5 SS events of SSW. Crosses indicate statistically significant regions at the 90% confidence level.

Figure 8. Zonal mean zonal wind anomaly (shading) and climatological December–February (DJF) mean and zonal-mean zonal wind (contours) based on MERRA data. The results from top to bottom are shown for DD, DS, and SS types, respectively, averaged over (a)–(c) days -20 to -5, (d)–(f) days -5 to +10, and (g)–(i) days +10 to +25. The bold solid and dashed–dotted contours denote zero and negative wind speeds. The contour interval is 7 m s^{-1}. Crosses indicate the statistically significant region at the 90% confidence level. The green contour in Figs. 8b and 9c shows the wind anomaly using the combined DS+SS type.

Figure 9. Anomalies of meridional eddy heat flux averaged over 45°–75°N at 100 hPa based on NCEP-NCAR data for (a) DD, (b) DS, and (c) SS types. The black line denotes anomalies from the total

eddies, and the orange and blue lines denote contributions by zonal waves 1 and 2, respectively. The bold solid part of each line indicates that the heat flux anomaly is significantly different from zero at the 90% confidence level.

Figure 10. GPH anomaly (shading) and climatological DJF mean values (contours) based on NCEP–NCAR data averaged over days -45 to 0. The GPH is averaged for latitude belts 45°N –75°N. The results are shown for (a)–(c) DD, (d)–(f) DS, and (g)–(i) SS types. From top to bottom, the total anomaly, wave-1 anomaly, and wave-2 anomaly are given. The bold solid and dashed–dotted contours denote zero and negative values. The contour interval is 80 m. Crosses indicate the statistically significant region at the 90% confidence level.

Figure 11. (a)-(f) SLP anomaly (shading) and zonal perturbation of DJF mean climatological values (contours) based on NCEP–NCAR data. The left and right panels show features averaged from days -45 to 0, and 0 to +45, respectively. From top to bottom, DD, DS, and SS types are shown. (g) Difference between (b) and (c). The dashed–dotted contour denotes negative values. The contour interval is 6 hPa, and zero contour is omitted. Crosses indicate statistically significant regions at the 90% confidence level.

Figure 12. Same as Fig. 7 but for the PCH anomaly calculated by using the WACCM results for (a) 64 DD types, (b) 31 DS types, and (c) 8 SS types.

Figure 13. Same as Fig. 7 but for the PCH anomaly calculated by using the WACCM results for (a) 55 DD types, (b) 36 DS types, and (c) 12 SS types. Daily GPH averaged over 50°N-60°N at 10 hPa used for classifying SSW type.

Figure 14. Same as Figs. 8a–c but for WACCM data.

Figure 15. Differences between zonal-mean zonal wind anomalies averaged from day -20 to -5 from WACCM results for (a) DD and DS, (b) DD and SS, and (c) DS and SS. Contour interval is 3 m s^{-1}. Green crosses and solid circles indicate statistically-significant region at 90% and 95% confidence level, respectively. Statistical significance is calculated using the Student's t-test.

Figure 16. Composite differences of zonal-mean zonal wind averaged over 50°N–70°N between DD and DS events from MERRA (DD minus DS). Gray horizontal and vertical lines denote the 10 hPa level and central day, respectively. The contour interval is 3 m s^{-1}. Pink crosses indicate statistically significant regions at 95% confidence level. Dashed-dotted contours denote negative values.

Figure 17. Zonal-mean zonal wind anomaly averaged over 50°N-70°N for DS type from MERRA data. Contour interval is 3 m s^{-1}. Pink crosses indicate statistically significant regions at 95% confidence level. Dashed-dotted contours denote negative values.

Figure 18. (a) Time series of 3-day running-mean NCEP/CPC NAO index. Blue and orange lines denote DD and DS SSW types,

respectively. The bold black solid part of each line with crosses indicates statistically significant periods at 95% confidence level. (b) Scatter plot of CPC NAO index occurring during the two SSW types. The NAO index is averaged over days -49 to -21. The mean NAO index for each type is represented by a closed circle with an error bar indicating one standard deviation. A filled circle denotes a statistically significant value at 95% confidence level.

Figure 19. NCEP-NCAR GPH anomalies at 500 hPa averaged over days -49 to -21 for (a) DD and (b) DS types. NCEP-NCAR GPH anomalies at 1000 hPa averaged over days -49 to -21 for (c) DD and (d) DS types. The contour interval is 20 m. Bold contours and pink dots indicate statistically significant regions at 95% confidence level.

Figure 20. GPH wave-1 anomalies (shading) and climatological DJF-mean value (contour) based on MERRA data averaged over (a) and (b) days -49 to -21 and (c) and (d) days -21 to 0 for (top) DD and (bottom) DS types. The GPH is averaged for latitude belts 45°N–75°N. Solid and dashed-dotted contours denote positive and negative values, respectively. The color intervals are 50 m and contour intervals are 120 m. Pink crosses indicate statistically significant regions at 95% confidence level.

Figure. 21. Zonal-mean zonal wind anomalies (shading) averaged over days -49 to -21 for (a) DD and (b) DS types and climatological DJF mean value (contour) based on MERRA data. Contour

interval is 7 m s^{-1}. Crosses indicate the statistically significant region at 95% confidence level.

Figure 22. (a)–(h) GPH anomalies at 500 hPa averaged over 7 days from days -28 to 0 for DD and DS types following positive NAO phase and climatological DJF-mean value (contour) based on NCEP-NCAR data. (a)–(d) wave-1 anomaly and (e)–(h) wave-2 anomaly. The color interval is 9 m and contour interval is 35 m. Purple and green contours denote positive and negative values, respectively. The thick solid contour denotes zero value. Pink dots indicate significantly regions at 95% confidence level. (i) Anomalies of meridional eddy heat flux averaged over 45°N–75°N at 100 hPa for DD and DS types following the positive NAO phase based on NCEP-NCAR data. The blue and orange lines denote contributions by zonal waves 1 and 2 to total eddies. Pink crosses and thick solid part of each line indicate significantly regions at 95% and 90% confidence level, respectively.

Figure. 23. Same as in Fig. 22 but for negative NAO.

Figure 24. Same as Fig. 16 but for WACCM zonal wind.

Figure 25. Same as Fig. 18 but for WACCM NAO index.

Figure 26. (a) and (b) Same as Figs. 19a and 19b but for WACCM GPH anomalies averaged over days -35 to -14.

Table 1. SSW events identified from NCEP–NCAR (columns 2 and 3) and MERRA (columns 4 and 5) datasets and from CJ11 (columns 6 and 7) and CP07 (column 8). Letters in italics indicate SSWs

found in only one dataset. Bold letters denote different classification among the studies.

Table 2. Number of each SSW type occurring in different latitude belts based on NCEP–NCAR and MERRA data. Column 7 shows the ratio of DD to DS+SS types.

Table 3. Same as Table 2 but for WACCM results.

1. Motivation and objectives

Since it was first observed in 1952, sudden stratospheric warming (SSW) has been a stratospheric climate variability of major interest in the Northern Hemisphere (NH) winter season. This phenomenon is characterized by a rapid increase in polar stratospheric temperature and an abrupt decrease in circumpolar zonal wind; various methods of defining SSW have been detailed by Butler et al. (2015).

The change in zonal flow is accompanied by deformation in the shape of the polar vortex. The changes in the vortex state are the response of a dynamic process such as wave breaking (McIntyre and Palmer, 1983; Baldwin and Holton, 1998). Therefore, SSW type can be distinguished depending on the vortex shape to understand the variability in the dynamic characteristics associated with the SSW. The terms of "displacement" and "split" were used to describe the basic features of the polar vortex shape identified from the observation instruments during the SSW period (Labitzke, 1968; Labitzke, 1978). More than half of SSW events are categorized as displacement type because the center of polar vortex shifts toward lower latitudes. The other SSW event type is known as split type because the polar vortex splits into two vortices of similar size and strength. This displacement and splitting of the polar vortex are regarded as wave-1 and wave-2 types, respectively.

Yoden et al. (1999) used the relative strength of stratospheric planetary waves to classify the SSW type. Bancalá et al. (2012) and Barriopedro and

Calvo (2014, hereafter BC14) also used dominant waves to classify SSW. Charlton and Polvani (2007, hereafter CP07) used absolute vorticity on the pressure surface to objectively classify the type; this method was also used by Cohen and Jones (2011, hereafter CJ11). Mitchell et al. (2013) suggested a classification algorithm by using the area, shape, and location of the vortex. Lawrence and Manney (2018) introduced computer vision techniques to analyze the geometry of the Arctic polar vortex and showed the applicability of this method as an analysis tool.

A significant factor in determining the type appears to be the time at which the SSW is characterized. Several studies, including Yoden et al. (1999) and Bancalá et al. (2012), focused on the wave evolution features exhibited during the prewarming phase, whereas CP07 considered vortex separation during the period comprising both the prewarming and postwarming phases to classify the type.

A comparison between the Bancalá et al. (2012) classification results and those of CP07 shows that all wave-2 types correspond to the split type but not all wave-1 types match the displacement type. This is because some wave- 1 types lead to a split event during the postwarming phase (Bancalá et al. 2012). This type has been referred to as hybrid type (O'Neill 2003), mixed type (Mitchell et al. 2013), wave-1 amplification-related splitting event (BC14), and wave-1 splitting event (Bancalá et al. 2012). Because the mixed type is influenced by timing, which is considered to characterize the SSW type, the group to which it belongs may vary among studies.

Nevertheless, the impact of the mixed type on composite analysis studies, which is used to identify general features based on SSW type, has not been examined in detail.

In the process of analyzing the data to identify the dynamical features of SSW events based on the traditional classification of the two types, we found two distinctive groups of SSW among the split-type events. Thus, in contrast to the previous studies, we intend to classify SSW into three types considering its evolution before and after the central day of the warming event. To accomplish this, a simple objective algorithm that considers wave amplitude is used. Different characteristics, depending on the SSW type, are identified by using reanalysis data and model results. As discussed subsequently, the differences among these three types are more robust than those reported between the traditional displacement and split types. Therefore, considering these three types are distinctively different from each other, it is more appropriate to classify SSWs into three types rather than two types to achieve a better understanding of SSW events.

Although the type of SSW is classified according to the polar vortex shape in this study, SSW can be characterized differently depending on the issues being focused. The classification of SSW events proposed in Kodera et al. (2016) is based on the upward propagation property of planetary waves and focused on the temporal evolution of the stratospheric circulation during the recovery phase of the SSW. Nakagawa et al. (2006) classified the SSW events into two groups based on the propagation of stratospheric polar temperature

anomalies into the troposphere, as determined from 30-day averaged anomalies in polar temperature at 500 hPa.

The methods for determining the polar vortex state continue to evolve. The machine learning approaches such as clustering algorithms have been applied to identify the dominant spatial patterns and temporal evolution of polar vortex. The cluster analysis enables to study the different vortex states based on their spatial structure without suffering of researcher subjectivity (Kretschmer et al. 2018, Krinitskiy et al. 2019). Therefore, we do not mean that a three-type classification is the only way to characterize vortex state and SSW and that the number of types should be limited to three. We aim to show that traditional split-type events consist of two groups with different dynamical characteristics.

Since SSWs are known to be related to variability in tropospheric circulation and weather (Baldwin and Dunkerton, 1999, 2001; Thompson et al., 2002), predicting the occurrence of SSWs is an important issue in sub-seasonal to seasonal forecasting (Karpechko et al., 2018; Taguchi, 2018; Rao et al., 2019). The ability to forecast stratosphere-troposphere coupling after warming events could be improved by understanding what mechanisms influence the change in the stratospheric polar vortex in advance. Thus, many studies have been performed toward understanding the differences in various SSW precursory patterns related to weakening and breaking of polar vortexes. These studies, however, have analyzed SSWs based on two traditional types, “vortex displacement type” and “vortex split type”

(CP07), or involved a case study (Attard et al., 2016; Cohen and Jones, 2011; Martius et al., 2009; Naujokat et al., 2002). In contrast, we apply the three-type classification to investigate precursors.

Baldwin et al. (1994) showed that the zonal-mean stratospheric polar vortex is positively correlated with the North Atlantic Oscillation (NAO). Ambaum and Hoskins (2002) also showed that the stratospheric jet is strengthened by an increase in the NAO owing to the increased equatorward refraction of upward-propagating Rossby waves. However, how the NAO conditions relate to the subsequent development of different SSW types has not yet been reported in the literature. Therefore, we aim to investigate the role of the NAO in determining SSW type after the onset.

In section 2, the reanalysis data and the model used for simulation are described. In section 3, we suggest a method for classifying SSW events into three types, and we discuss the different features depending on the type using the reanalysis data and model results. Section 4 discusses how the NAO appears to act as a precursor for SSW type and a summary and discussion are presented in section 5.

2. Data and model

2.1 Data

The two datasets used for this analysis are the Modern Era Retrospective–Analysis for Research and Applications (MERRA) assimilated data (inst3_3d_asm_Cp; Rienecker et al. 2011) and National Centers for Environmental Prediction–National Center for Atmospheric Research (NCEP–NCAR) reanalysis data (Kalnay et al. 1996). From the MERRA data, zonal and meridional winds, air temperature, and geopotential height (GPH) were obtained with a horizontal resolution of 1.25° latitude × 1.25° longitude at 42 pressure levels from 1000 hPa to 0.1 hPa from 1 January, 1979 to 31 December, 2014. From the NCEP–NCAR data, zonal and meridional winds, air temperature, and GPH are presented with a horizontal resolution of 2.5° latitude × 2.5° longitude at 17 pressure levels from 1000 to 10 hPa and sea-level pressure from 1 January, 1957 to 31 December, 2014.

The climatological values were calculated daily from each variable based on the period 1979–2011 for MERRA and 1981–2010 for NCEP–NCAR and were smoothed by a 31-day running mean. In this study, all anomaly fields are defined by perturbations from these 31-day running mean climatological values. The results in this paper are insensitive to the dataset. To show changes in variables in the vertical direction, we display the results from MERRA, which have a higher vertical top than the other reanalysis dataset.

To characterize the strength and phase of the NAO, two daily NAO indices were downloaded from two websites. One from the NCEP/Climate Prediction Center (CPC) (https://www.cpc.ncep.noaa.gov/products/precip/CWlink/pna/nao.shtml) was constructed by projecting daily 500-hPa height anomalies over the Northern Hemisphere onto the loading pattern of the NAO, which is defined as the first leading mode in the rotated empirical orthogonal function analysis. The other index, from the National Oceanic and Atmospheric Administration (NOAA)/Earth System Research Laboratory (ESRL)/Physical Sciences Division (PSD) (https://www.esrl.noaa.gov/psd/data/timeseries/daily/NAO), was constructed by the difference between daily 500-hPa GPH anomalies averaged over two fixed domains (35°N–45°N, 70°W–10°W and 55°N–70°N, 70°W–10°W). Before computing the NAO index, 500-hPa height anomaly fields were reconstructed from the wave components of zonal wave numbers 1–10 in order to emphasize large-scale features. Both NAO indices from 1 July 1957 to 30 June 2014 were used. The modeled NAO index was calculated based on the ESRL/PSD method because of its relative simplicity.

2.2 Model

For model simulations, the Whole Atmosphere Community Climate Model (WACCM) was used. WACCM is the atmospheric component of the Community Earth System Model (CESM1.0.6) and includes all physical parameterizations of Community Atmospheric Model version 4 (Neale et

al. 2012). WACCM has a horizontal resolution of 1.9° latitude × 2.5° longitude at 66 hybrid pressure-sigma levels from the surface to 140 km in terms of log-pressure altitude with variable vertical resolution. The vertical coordinate was converted into a pressure coordinate with 43 levels from 1000 hPa to 0.0001 hPa (about 112.8 km) before analysis. For the lower boundary conditions, sea surface temperature and sea ice data were obtained from the monthly Hadley Centre Sea Ice and Sea Surface Temperature dataset (Rayner et al. 2003). For chemical conditions, the configurations of perpetual 2000 AD and specified chemistry (SC) were used. The SC–WACCM is known to reduce the computational cost to approximately one-half that of WACCM (Smith et al. 2014). No significant differences were noted in the simulation of the surface, tropospheric, and stratospheric climate compared with WACCM values under pre-industrial conditions (Smith et al. 2014).

This model has been used in previous studies and has produced the major SSW events in the NH at frequencies comparable to those revealed by observations (Richter et al. 2010; Limpasuvan et al. 2011; de la Torre et al. 2012; Marsh et al. 2013).

In the WACCM simulations, focus is placed on the internal dynamics of the stratosphere under the climatological boundary conditions. The model excluded interannual variability originating from the troposphere, such as El Niño–Southern Oscillation (ENSO) and sea-ice melting. The monthly sea surface temperature and sea ice data from 1981 to 2010 were averaged, and

their annually varying climatological values were prescribed repeatedly every year in the model. For model result in Section 3, the model was run for 211 years, and 200 boreal winters (1 October through 31 March) from the last 201 years were analyzed. For model result in Section 4, the model was run for 361 years, and 350 boreal winters from the last 351 years were analyzed. In all analyses, Student's t-test was applied for statistical significance testing.

3. Type Classification of SSW based on pre- and postwarming periods

3.1 Classification of SSW type

To classify the major SSW events in this study, we used a common definition based on the zonal mean zonal wind at 10 hPa and 60°N during the boreal winter season. A zonal wind reversal from westerly to easterly indicates a major SSW event; the first day of the wind reversal is defined as the central day of the SSW. To distinguish SSW from stratospheric final warming, the central day should appear at least 10 days before the end of March, and the westerly zonal wind should recover before the end of March. On this basis, 37 and 25 major SSW events were identified from the NCEP–NCAR reanalysis from 1957 to 2014 and from the MERRA data from 1979 to 2014, respectively. The frequency of the SSW occurrence per year was 0.65 for NCEP–NCAR and 0.7 for MERRA, which is similar to that found in CP07 (0.62).

3.1.1 Classification algorithm

Classification of SSW type requires consideration of the time evolution of the vortex shape. Waugh (1997) represented polar vortices by using elliptic shapes. A widely accepted method suggested by CP07 carefully considers the two-dimensional development of SSW. Although their sophisticated classification method has been continually used and developed (Cohen and Jones 2012; Mitchell et al. 2013; Lawrence and Manney 2018), it requires complex calculations. In order to avoid these computational complexities, we used simple harmonic analysis to obtain results very similar to those from previous studies, such as CP07. Because

the SSW types of displacement and split show dominant patterns of wave 1 and wave 2, respectively, we began the classification based on the amplitude of zonal waves 1 and 2 by using harmonic analysis. The process is described as follows.

1. For an individual SSW event, the daily GPH averaged over 55°N–65°N at 10 hPa was decomposed by harmonic analysis to obtain the amplitude for zonal waves 1 and 2. We examined the frequency of each type for the five latitude belts of 10° width, shifting 5° from 45°N–55°N to 65°N–75°N. The band of latitude 55°N–65°N was selected because the classification results based on this latitude band are the closest to those reported by CP07. The sensitivity of the SSW type classification to these five latitude bands is discussed in Section 3c.

2. This analysis was conducted for a period of 21 days, from 10 days before the central day to 10 days afterward. We tested the sensitivity to the period of analysis by changing the pre- and post-event periods from 10 to 15 days. However, the analysis period did not appear to be crucial for determining the type, as noted in Section 3c. Throughout the 21 days of analysis, if the amplitude of wave 2 was larger than that of wave 1 on any day, the event was regarded as a wave-2 type; otherwise, it was regarded as a wave-1 type. Although the names “wave 1” and “wave 2” were used temporarily for convenience, these two types are, in fact, very similar to the displacement and split types, respectively. Their similarities are shown in Table 1.

The amplitudes of waves 1 and 2 were obtained through the process

described above by using MERRA data. Their ratios are shown in Fig. 1 for SSW events from 14 days before the central day (0) to 14 days afterward. For the 13 wave-1-type events (Fig. 1a), from day –10 to day 10, the ratios exhibited small variations and imply that the amplitude of wave 2 was relatively small. On the contrary, for the 12 wave-2 types (Fig. 1b), the amplitudes were sometimes significantly larger than those of wave 1. The most prominent example is the 24 January, 2009 SSW event, represented by the dashed line in Fig. 1b. Moreover, for the wave-2 type shown in Fig. 1b, two peaks occurred in the composited ratio. These double peaks imply that some of the SSW events had a large wave 2 either before or after the central day or both.

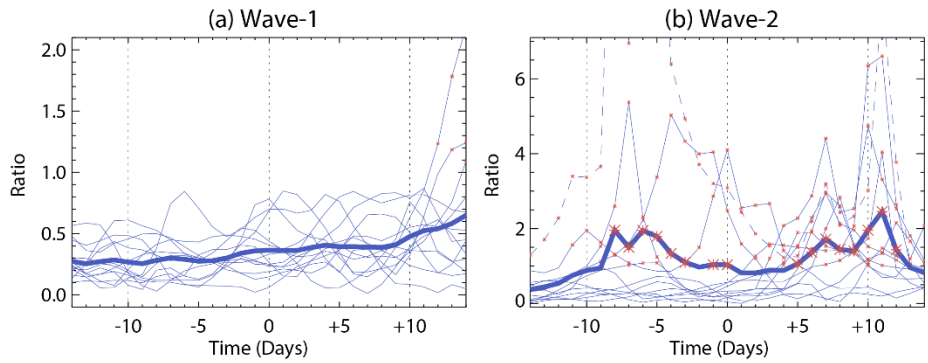

Figure 1. Temporal evolution of the amplitude ratio of wave 2 to wave 1. Thin lines represent individual SSW events, and the thick line shows their composite mean. Ratios larger than 1.0 are shown with a red asterisk. (a) 13 wave-1 type SSW events; (b) 12 wave-2 type SSW events. The dashed line in (b) corresponds to an SSW event occurring on 24 January 2009 with maximum ratios of 14.9 on day –8 and 8.3 on day +11. It should be noted that the range of the vertical axis is different.

3.1.2 Objective definition of the displacement-split type

To determine whether all of the SSW events in Fig. 1b had similar characteristic features, the wave-2 types were separated into two groups, as shown in Fig. 2. Fig. 2a shows the cases in which a ratio larger than the threshold value of 1 was observed between day 0 and day +10, i.e., only after the central day. In these 7 cases out of 12, behavior similar to that shown in Fig. 1a, before the central day, is presented in Fig. 2a. Fig. 2b shows that five SSW events had a ratio larger than the threshold value of 1 before the central day (from −10 to −1). Based on the temporal evolution of the ratio during the pre-warming and post-warming phases given in Fig. 2, we classified the SSW events in Fig. 2a as displacement–split (DS) type and those in Fig. 2b as split–split (SS) type. Although the DS type is explicitly defined here objectively, it has been described previously by other names, as discussed in the Introduction. In the DS type, the composited ratio gradually increases after the central day and exceeds the threshold value of 1 after about five days. The increase in the ratio during the SSW events is related to the fact that the wave-1 amplitude decreases more than the wave-2 amplitude increases (not shown). On the contrary, the large ratio in the SS type is attributed to the development of wave 2. Among the SS types (Fig. 2b), a single SSW event was noted in which the ratio was below 1 for the post-warming phase (day +1 to +10). This event could have been classified as split–displacement (SD) type. However, because it was observed only once in both the MERRA and NCEP–NCAR data (24 February, 2007), this type will not be discussed further.

In the name of each type, the first and second characters represent both the dominant wavenumber and the shape of the polar vortex before and after the central day. D represents wave 1 and vortex displacement, and S denotes the wave 2 and vortex split. As shown in Fig. 1a, wave 1 persisted both before and after the central day and was classified as displacement–displacement (DD) type by applying the same naming scheme. Hereafter, the above three types will be used for classification.

To show the validity of separating the wave-2 type into DS and SS, a typical SSW event was selected from each type to reveal the evolution of the synoptic structure depending on the type. Fig. 3 shows the temporal evolution of the GPH at 10 hPa for the three different SSW types. The SSW events of 22 February, 2008, 8 December, 1987, and 1 January, 1985, were selected to represent DD, DS, and SS type, respectively. As shown in Fig. 2b, the most prominent SS event was the SSW occurring on 24 January, 2009. This case exhibited exceptional development of wave 2 compared with the other SS events and has been extensively studied (Manney et al 2009; Harada et al 2010; Ayarzagüena et al. 2011; Coy et al 2011; Albers and Birner 2014; Kodera et al 2015, 2016; Wang et al 2016). However, because this case can be considered as an exception to the typical SS type, we selected a different SSW event, occurring in 1985, to show a more typical example.

The DD-type SSW event shown in Fig. 3a is characterized by a single displaced polar vortex shaded in blue and a wave-1 pattern throughout the

SSW period. The DS type in Fig. 3b shows a pattern similar to the DD type before the central day, with wave-1 characteristics and a displaced vortex. During the post-warming period, however, the vortex moved westward and split into a wave-2 pattern. In the SS type shown in Fig. 3c, the polar vortex shows a wave-2 pattern throughout the SSW period. As expected from the name of each type, DD and DS types share similarities during the pre-warming period, and the DS and SS types resemble each other during the post-warming periods. It can be confirmed that the number of the wave between the dominant planetary waves 1 and 2 is consistent with the shape of the polar vortex and that the DS type should be separated from the SS type. An exception was observed on day 5 in Fig. 3c in which the structure of the SS type, was rather similar to a wave-1 pattern. This occurred because the wave-2 activity weakened temporarily with the minimum on day 5 (Fig. 4).

To show a clear distinction between the SS and DD types prior to the SSW event in Figs. 3a and 3c, their differences in zonal mean zonal wind anomaly are exhibited in Fig. 5. The differences in Figs. 5a and 5b are based on NCEP–NCAR, and those in Fig. 5c are based on MERRA. The data in Figs. 5a and 5b are based on a different period. However, all three panels of Fig. 5 share remarkable similarities regardless of the datasets and data period, showing negative values at high latitudes and positive differences at midlatitudes from the surface to the stratosphere.

To examine the effect of DS type on composite analysis studies, the

differences in zonal mean zonal wind anomaly between the DD type and DS+SS type are shown in Fig. 6. This figure shows the differences between the displacement and split types as determined in previous studies; Fig. 6a can be compared with Fig. 7g of CP07, which uses the same dataset and analysis period. Figs. 6a and 6b use different analysis periods, and the results differ significantly. This shows that the differences based on the two conventional types are dependent on the analysis period. The differences during the 1958–2002 period (Fig. 6a) are similar but weak compared with those in Fig. 5, and the negative differences over the polar region in Fig. 6a disappeared for the 1979–2014 period in Fig. 6b. This inconsistency between Figs. 6a and 6b have occurred because the DS type was included in the calculation. Characteristic features of the DS type in the 1958-2002 period seem to be different from those in the 1979-2014 period. In such a case, the DS type should be explicitly separated from other split-type events and should have its own classification.

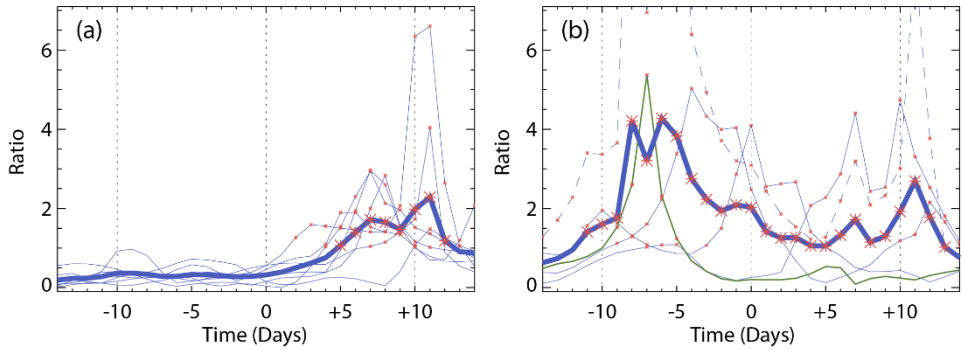

Figure 2. Same as in Fig. 1 but for (a) seven DS types and (b) five SS types. The dashed line and the green line in (b) correspond to SSW events occurring on 24 January 2009 and on 24 February 2007, respectively. DS and SS types are defined in the manuscript.

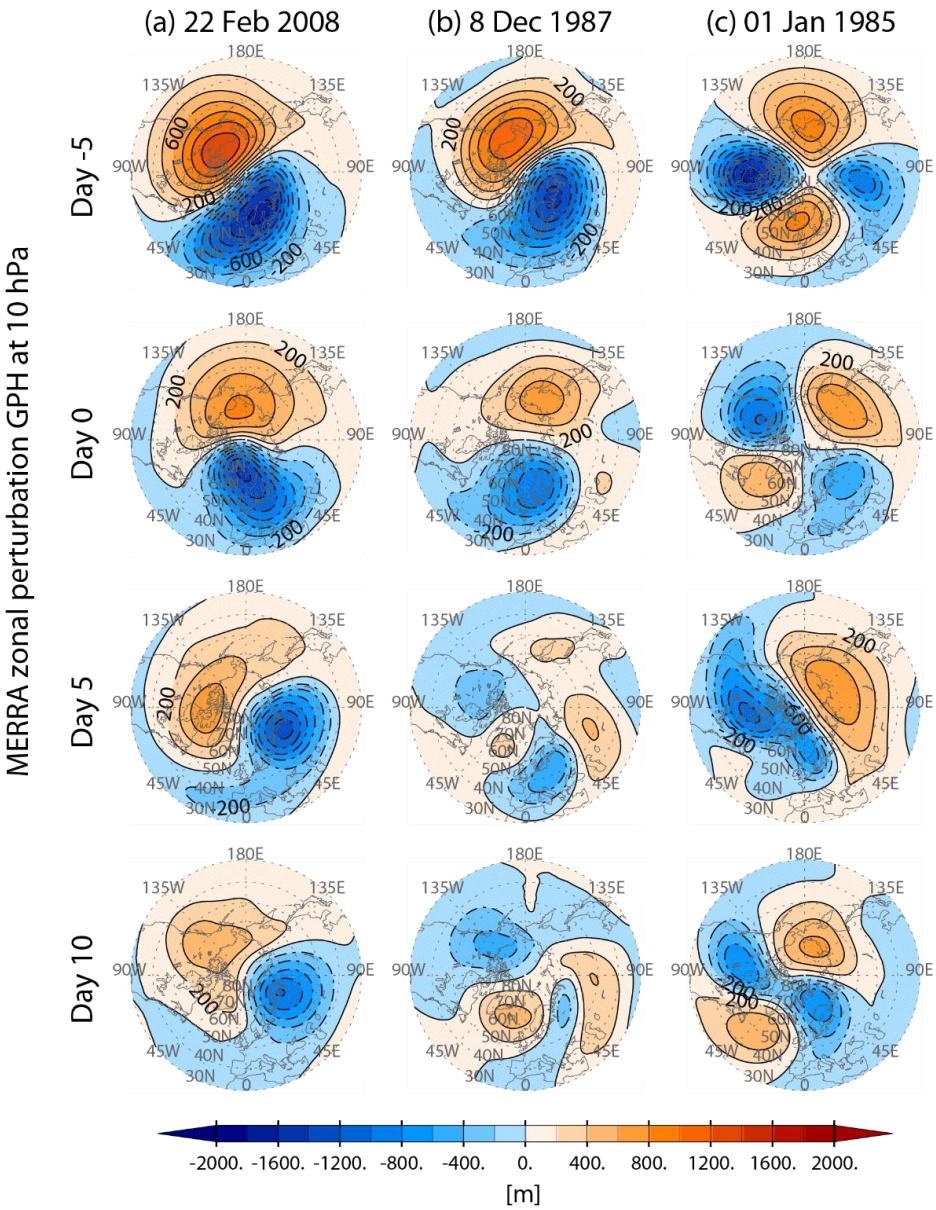

Figure 3. Zonal perturbation GPH at 10 hPa with a five-day interval based on MERRA data. (a) DD-type warming on 22 February 2008; (b) DS-type warming on 8 December 1987; (c) SS-type warming on 1 January 1985. The contour interval is 200 m.

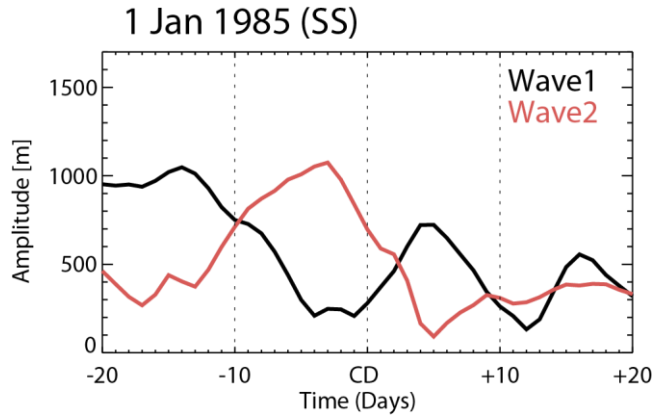

Figure 4. Temporal evolution of amplitude of waves 1 (black) and 2 (red) for the SS-type SSW in 1985 (Fig. 3c) from day -20 to day 20.

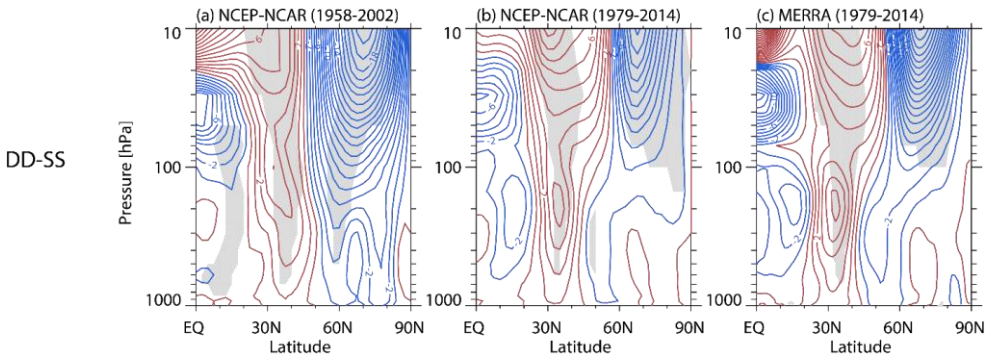

Figure 5. Differences in zonal mean zonal wind anomalies averaged from days -20 to -5 between DD and SS types for (a) 1958–2002 based on NCEP–NCAR data, (b) 1979–2014 based on NCEP–NCAR data, and (c) 1979–2014 based on MERRA data. The numbers of DD- and SS-type events are (a) 16 and 5, (b) 11 and 5, and (c) 13 and 5. The contour interval is 1.0 m s^{-1}. The blue and red contours indicate negative and positive differences, respectively. Gray shading indicates the region of statistical significance at the 90% confidence level.

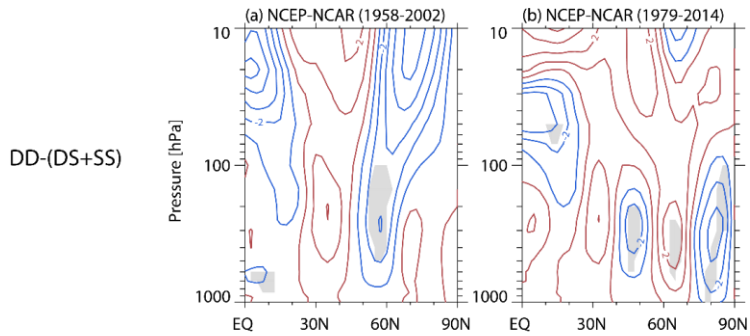

Figure 6. Same as Fig. 5 but for differences between DD and DS+SS types. The numbers of DD- and DS+SS-type events are (a) 16 and 12 and (b) 11 and 11, respectively.

3.1.3 Comparisons with other studies

The central days and types of SSW events identified from NCEP–NCAR and MERRA data by using the method described in the previous section are listed in Table 1 (columns 2–5). The differences between the classification results from both datasets were negligible. To compare our classification with other well-known classifications, the results obtained from CJ11 are shown. It should be noted that CJ11 used the method of CP07. Subjective classification reported by CP07 is also included in Table 1 (column 8). The notations "D" and "S" used by CJ11 and CP07 correspond to our DD and combined DS+SS, respectively.

According to our classification method, 20 DD, 10 DS, and 7 SS types were identified from NCEP–NCAR data (1957–2014), and 13, 7, and 5 were identified from MERRA data (1979–2014), respectively. The ratio of DD type to DS+SS type from NCEP–NCAR and MERRA data was about 1.18 and 1.08, respectively. The ratio is close to that reported by CP07 from 1957 to 2002, at 1.18. This shows that the results of our SSW-classification algorithm by wave amplitude are very similar to those resulting from the method of CP07.

The bold letters in Table 1 denote the SSW cases of different classifications from CJ11 (column 7). These four cases, represented in Table 1 as No. 28 (15 December, 1998), 29 (25 February, 1999), 38 (21 January, 2006), and 39 (24 February, 2007), were investigated closely by comparison with the results of previous studies and analysis of the vortex shapes by

GPH.

Concerning the case No. 28, Kodera et al. (2016) demonstrated two separate vortices in GPH and the relative vorticity at 10 hPa by using reanalysis data. This case was also described by Mitchell et al. (2013) as a mixed event based on the distribution of potential vorticity. No. 29 was classified as DD type in our algorithm and was considered as a displacement type in Mitchell et al. (2013). However, in the reanalysis data, two separate vortices were identified after the central day. The wave-2 amplitude also increased gradually near the central day until the maximum value appeared after the central day (not shown). However, because the wave-2 amplitude was smaller than that of wave 1, this case was classified as DD type. No. 38 was classified as DD type by our criteria. Manney et al. (2008) considered it to be a wave-1 event based on the potential vorticity map calculated using satellite data, and Manney et al. (2009) regarded it as displacement type. No. 39 is a rare case of SD type.

By using our simple method of wave amplitude calculation, we classified the SSW events as shown in Table 1. Of four cases of different classifications, only one case, No. 29, was subtle; thus, our classification method appears to be effective for the other three cases.

We examined the frequency of each type for the five latitude belts of 10° width, shifting 5° from 45°N–55°N to 65°N–75°N for the two reanalysis datasets. Table 2 shows the number of each SSW type according to the

amplitude changes of wavenumbers 1 and 2 at the different latitudes. The ratio of DD to DS+SS types increases with latitude because the wave-2 amplitude decreases with latitude. For the belt of 55°N–65°N, the ratio of DD type to DS+DS type was 1.18 for NCEP-NCAR data for 1957-2014, and 1.08 for MERRA data for 1979-2014, respectively; these results are similar to those reported by CP07.

We also tested the sensitivity of the classification type to the analysis period by changing the pre- and post-event periods from 10 to 15 days. Although the number of SS-type events remained the same, the number of DD- and DS-type events changed from 13 to 10 and from 7 to 10, respectively, owing to an increase in wave-2 activity after day +10. The identification and separation of the SS type from other types appears to be robust regardless of the analysis period.

Table 1. SSW events identified from NCEP–NCAR (columns 2 and 3) and MERRA (columns 4 and 5) datasets and from CJ11 (columns 6 and 7) and CP07 (column 8). Letters in italics indicate SSWs found in only one dataset. Bold letters denote different classification among the studies.

	NCEP-NCAR		MERRA		CJ11		CP07
No.	Central day	Type	Central day	Type	Central day	Type	Type Subjective
1	30 Jan 1958	SS			30 Jan 1958	S	S
2	30 Nov 1958	DD			30 Nov 1958	D	D
3	16 Jan 1960	DD			16 Jan 1960	D	D
4	-	-			*23 Mar 1965*	*S*	*S*
5	8 Dec 1965	DD			8 Dec 1965	D	D
6	24 Feb 1966	DS			24 Feb 1966	S	S
7	-	-			*8 Jan 1968*	*S*	*S*
8	27 Nov 1968	DD			27 Nov 1968	D	D
9	14 Mar 1969	DD			13 Mar 1969	D	D
10	2 Jan 1970	DD			2 Jan 1970	D	D
11	17 Jan 1971	DS			17 Jan 1971	S	S
12	20 Mar 1971	DD			20 Mar 1971	D	D
13	2 Feb 1973	DS			2 Feb 1973	S	S
14	*13 Mar 1974*	*DD*			-		-
15	*15 Mar 1975*	*DD*			-		-
16	*12 Mar 1978*	*DS*			-		-
17	22 Feb 1979	SS			22 Feb 1979	S	S
18	29 Feb 1980	DD	29 Feb 1980	DD	29 Feb 1980	D	D
19			*4 Mar 1981*	*DS*			
20	4 Dec 1981	DD	4 Dec 1981	DD	4 Dec 1981	D	D
21	24 Feb 1984	DD	24 Feb 1984	DD	24 Feb 1984	D	D
22	2 Jan 1985	SS	1 Jan 1985	SS	2 Jan 1985	S	S
23	23 Jan 1987	DD	23 Jan 1987	DD	23 Jan 1987	D	D
24	8 Dec 1987	DS	8 Dec 1987	DS	8 Dec 1987	S	S
25	14 Mar 1988	SS	14 Mar 1988	SS	14 Mar 1988	S	S

26	22 Feb 1989	SS	21 Feb 1989	SS	22 Feb 1989	S	S
27			*5 Feb 1995*	*DD*			
28	15 Dec 1998	**DS**	15 Dec 1998	**DS**	15 Dec 1998	**D**	**D**
29	25 Feb 1999	**DD**	26 Feb 1999	**DD**	25 Feb 1999	**S**	**S**
30	20 Mar 2000	DD	20 Mar 2000	DD	20 Mar 2000	D	D
31					*16 Dec 2000*	D	
32	11 Feb 2001	DS	11 Feb 2001	DS	11 Feb 2001	S	S
33	2 Jan 2002	DD	30 Dec 2001	DD	2 Jan 2002	D	D
34			*17 Feb 2002*	*DD*			
35	18 Jan 2003	DS	18 Jan 2003	DS	18 Jan 2003	S	
36	7 Jan 2004	DD	4 Jan 2004	DD	7 Jan 2004	D	
37	12 Mar 2005	DD	12 Mar 2005	DD			
38	21 Jan 2006	**DD**	21 Jan 2006	**DD**	21 Jan 2006	**S**	
39	24 Feb 2007	**SD**	24 Feb 2007	**SD**	24 Feb 2007	**D**	
40	22 Feb 2008	DD	22 Feb 2008	DD	22 Feb 2008	D	
41	24 Jan 2009	SS	24 Jan 2009	SS	24 Jan 2009	S	
42	9 Feb 2010	DS	9 Feb 2010	DS	9 Feb 2010	S	
43	7 Jan 2013	DS	6 Jan 2013	DS			

Table 2. Number of each SSW type occurring in different latitude belts based on NCEP–NCAR and MERRA data. Column 7 shows the ratio of DD to DS+SS types.

Data	Latitude	Type				Ratio
		DD	DS+SS	DS	SS	DD/(DS+SS)
NCEP–NCAR	45°N–55°N	14	23	14	9	0.61
	50°N–60°N	17	20	12	8	0.85
	55°N–65°N	**20**	**17**	**10**	**7**	**1.18**
	60°N–70°N	24	13	6	7	1.85
	65°N–75°N	23	14	8	6	1.64
MERRA	45°N–55°N	10	15	6	9	0.67
	50°N–60°N	11	14	6	8	0.79
	55°N–65°N	**13**	**12**	**7**	**5**	**1.08**
	60°N–70°N	14	11	6	5	1.27
	65°N–75°N	14	11	6	5	1.27

3.1.4 Characteristic features of the three SSW types

To analyze the characteristic features of the three SSW types, composite means were obtained by using both NCEP–NCAR and MERRA data. The results are insensitive to the dataset. Fig. 7 shows a time–height cross-section of the composite of the polar cap height (PCH) anomaly for each SSW type. Following Kim et al. (2014), the PCH anomaly was defined by the area-averaged GPH anomaly over the area north of 65°N and was normalized by its temporal standard deviation at each pressure level. The existence of a positive PCH anomaly corresponds to a weakened polar vortex.

Beginning on day –20, a positive PCH anomaly for the DD type (Fig. 7a) developed in the upper stratosphere and descended with time. The DS type (Fig. 7b) also showed the gradual descent of the positive PCH anomaly before the central day. The SS type (Fig. 7c) showed different characteristics from DD and DS types. The negative PCH anomalies were dominant from the surface to the lower mesosphere until day -15. From around day -5 sudden descent of positive PCH anomaly were shown along the whole column.

Prior to the central day, ascent of the positive PCH anomaly from the troposphere to the stratosphere was observed in both DS and SS types beginning on days –10 and –5, respectively; however, this phenomenon did not occur in the DD type. Afterward, the negative PCH anomaly descending from the upper to the middle stratosphere was larger for the DS

and SS types compared with that for the DD type. Considering all the observations presented in Fig. 7, DS share more similarities with DD than SS before the central day.

Fig. 8 shows the meridional cross-sections of the MERRA zonal mean zonal wind anomaly averaged over three periods for each type. During the pre-warming period (Figs. 8a–c), the anomalies of zonal wind showed significant differences among the types, particularly between DS and SS, as expected by the aforementioned observations. In the stratosphere over the polar region, a negative anomaly dominated in the DS type, whereas in the SS type, the anomaly pattern formed a dipole structure centered at middle latitude throughout the entire stratosphere. To show the differences between DS and SS types more clearly, the anomaly of the combined DS+SS type is represented by a green contour in Figs. 8b and 8c. If we calculated the anomaly for the conventional split type, that anomaly would be close to this green contour. The green contour line at the polar middle stratosphere does not share similarities with either DS or SS anomalies. Thus, the separation of the conventional split types into DS and SS types has been validated.

Near the central day, three types showed similar anomalies with each other in the extratropical stratosphere; negative anomalies were also noted in the troposphere. In the post-warming period, all three types are characterized by the shifting of positive anomalies from the low-latitude middle stratosphere to the polar upper stratosphere and mesosphere.

Among the three SSW periods shown in Fig. 8, the differences were most significant during the pre-warming period, particularly between the DS and SS types; the differences in the later periods were smaller.

The meridional eddy heat flux represents the vertical component of the Eliassen–Palm flux and serves as an indicator of the vertical flux of wave activity from the troposphere into the stratosphere. To identify the vertical propagation of the planetary wave, the area-weighted meridional eddy heat flux anomaly is presented in Fig. 9.

For all types, the positive heat flux anomaly began to increase about 20 days before the central day. The dominant wave component contributing to the total component differed among the types. In both DD and DS types, the wave-1 component accounted for most of the total component prior to the central day. The role of the wave-2 component was marginal throughout the period in the DD type, whereas it began to increase a few days before the central day in the DS type and dominated before the central day in the SS type. Moreover, the wave-1 component showed negative values after the central day in the SS and DS types.

In general, the DD and DS types showed similarities in total eddies and in the wave-1 component prior to the central day. We also calculated the composite mean of the meridional heat flux anomaly by using cases combining the DS and SS types (Fig. 9d). The results indicate that the wave-1 and wave-2 components are comparable and that the dominant wave

components are not clearly distinguishable, which is in contrast to that shown in Figs. 9b and 9c.

One noteworthy point for the SS type is that a significant precursory positive heat flux anomaly caused by the wave-1 component occurred near day –30. Most of the SS-type SSW events occurred in the second half of winter; and minor warming events were observed prior to the occurrence. This precursor might capture the associated upsurge of wave activity. Although precursor was less clear in the DS type, it has been identified in the split type reported by CP07.

To investigate the possibility of tropospheric influence on the stratospheric waves in Fig. 9, the tropospheric anomaly fields for each type were examined. Fig. 10 shows the zonal and vertical structure of the planetary wave anomaly averaged over the 45-day period prior to the central day. The vertical structure of the GPH anomaly field in the DS type (Fig. 10d) was similar to that in the DD type (Fig. 10a) and clearly differed from that in the SS type (Fig. 10g). In the DS and DD types, wave-1 anomalies were predominant (Figs. 10b, 10e). Their ridges and troughs shifted westward toward the upper level and were in phase with the winter climatological wave-1 pattern, which indicates that the planetary wave prior to the central day favors vertical propagation. The SS type exhibited a relatively weaker baroclinic structure, as was noted in previous studies (Martius et al. 2009; Matthewman et al. 2009). Because the wave-1 field for the SS type (Fig. 10h) exhibited negligible amplitude and was generally out

of phase, showing large temporal variability, the contribution was relatively small. However, the wave-2 anomaly developed in phase with the climatological wave 2 (Fig. 10i).

Fig. 11 shows the sea level pressure (SLP) anomaly averaged for the 45-day period before and after the central day. This figure can be compared with Fig. 1 of CJ11, in which the categories of the displacement and split types were used. Although the location of the positive anomalies in Eurasia differs in DD and DS types (Figs. 11a, 11b), the SLP anomaly of both DD and DS types shows that positive anomalies in northwest of the Siberian High along with negative anomalies associated with the Aleutian Low may have contributed to the formation of the wave-1 anomaly pattern in the stratosphere. On the contrary, for the SS type (Fig. 11c), the positive anomaly related to the Siberian High was weak, and a different positive anomaly was observed in the North Pacific region. This structure is favorable for wave-2 development (Martius et al. 2009; Nishii et al. 2011; CJ11). The spatial patterns in the SLP anomalies prior to the SSW event are consistent with that shown in Fig. 10. During the post-warming period, the composite structures of the three types in the SLP anomaly (Figs. 11d–f) were qualitatively similar to that shown in CJ11.

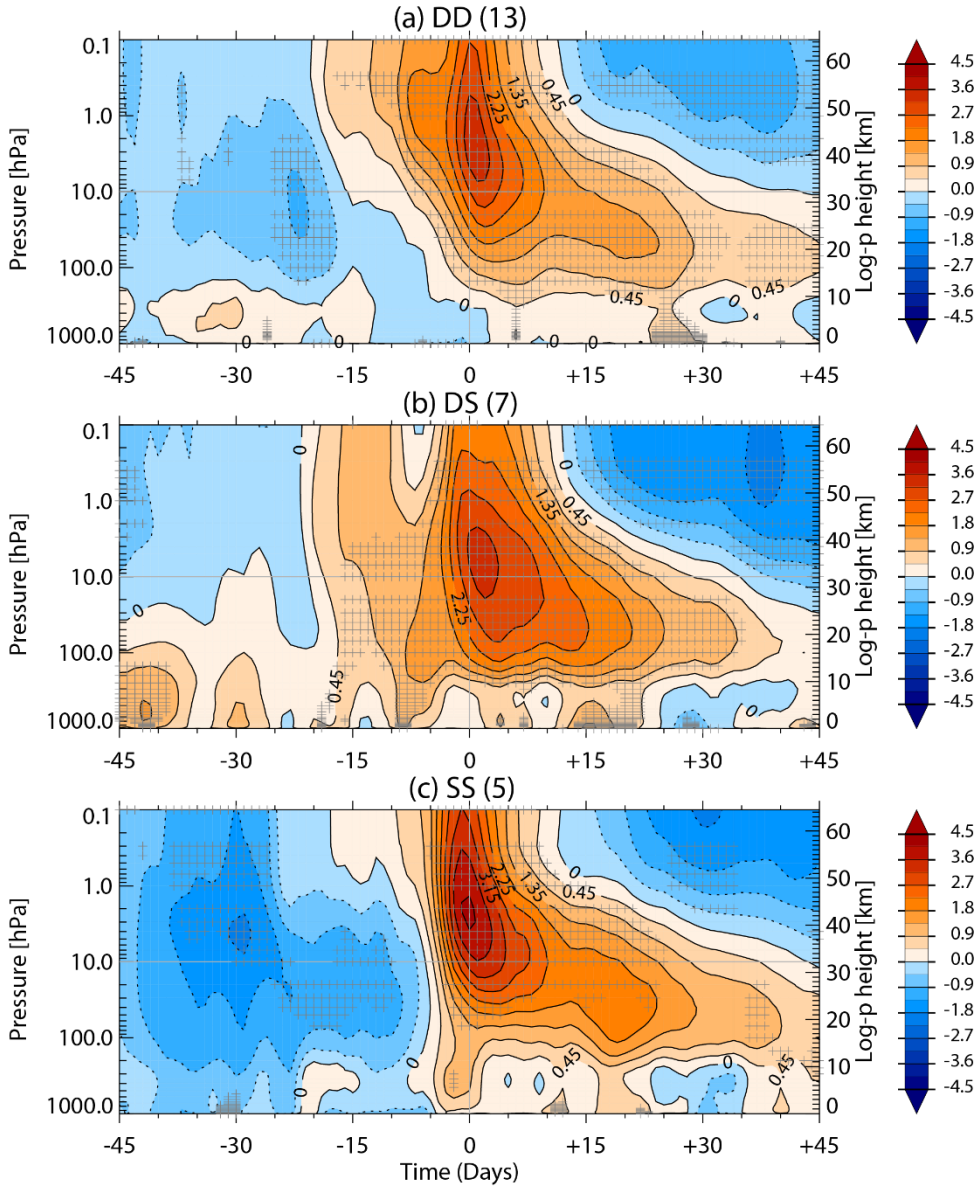

Figure 7. PCH anomaly based on the MERRA GPH anomaly averaged over 65°N–90°N for (a) 13 DD events, (b) 7 DS events, and (c) 5 SS events of SSW. Crosses indicate statistically significant regions at the 90% confidence level.

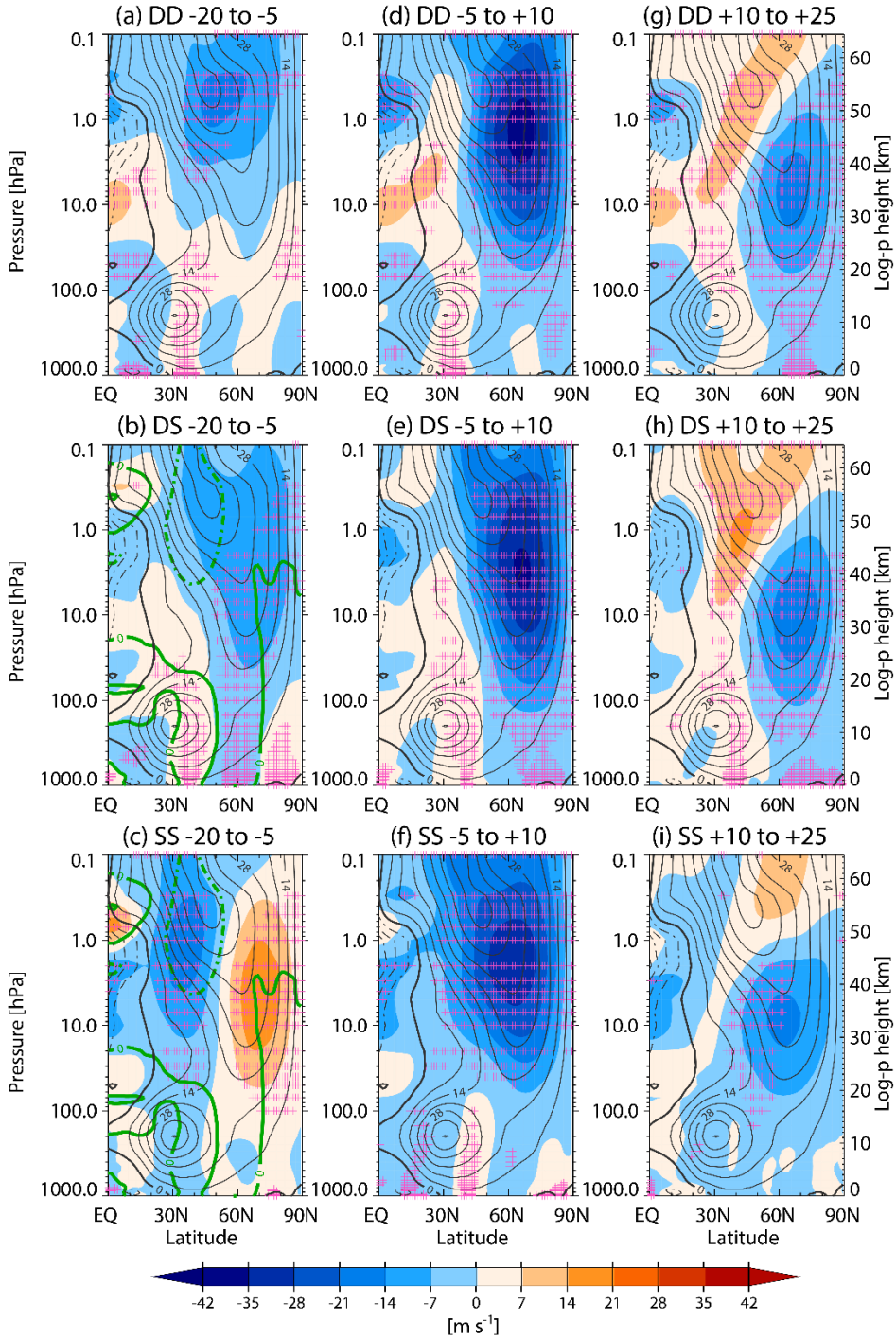

Figure 8. Zonal mean zonal wind anomaly (shading) and climatological December–February (DJF) mean and zonal-mean zonal wind (contours) based on MERRA data. The results from top to bottom are shown for DD,

DS, and SS types, respectively, averaged over (a)–(c) days -20 to -5, (d)–(f) days -5 to +10, and (g)–(i) days +10 to +25. The bold solid and dashed–dotted contours denote zero and negative wind speeds. The contour interval is 7 m s^{-1}. Crosses indicate the statistically significant region at the 90% confidence level. The green contour in Figs. 8b and 9c shows the wind anomaly using the combined DS+SS type.

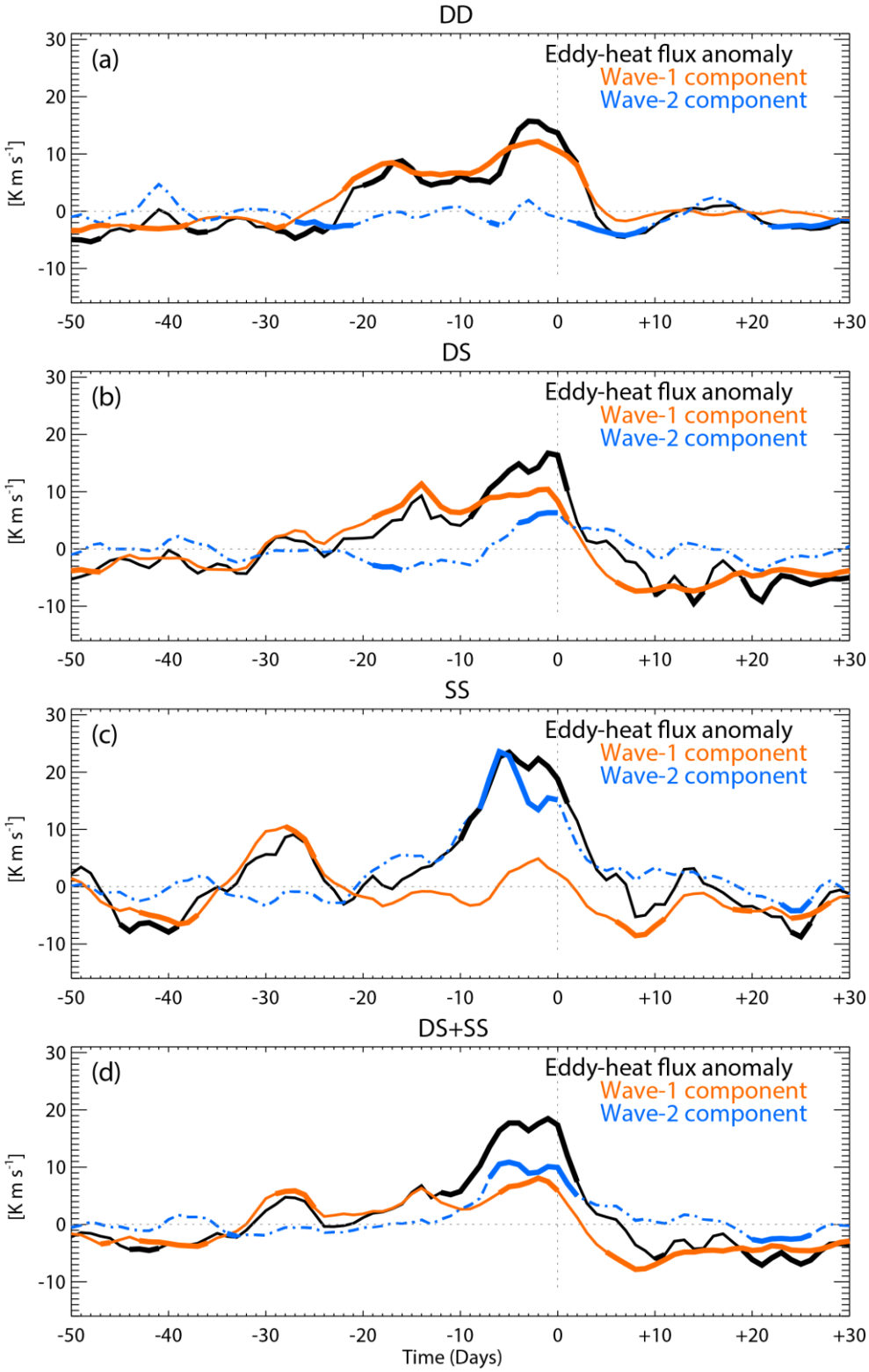

Figure 9. Anomalies of meridional eddy heat flux averaged over 45°–75°N

at 100 hPa based on NCEP-NCAR data for (a) DD, (b) DS, and (c) SS types. The black line denotes anomalies from the total eddies, and the orange and blue lines denote contributions by zonal waves 1 and 2, respectively. The bold solid part of each line indicates that the heat flux anomaly is significantly different from zero at the 90% confidence level.

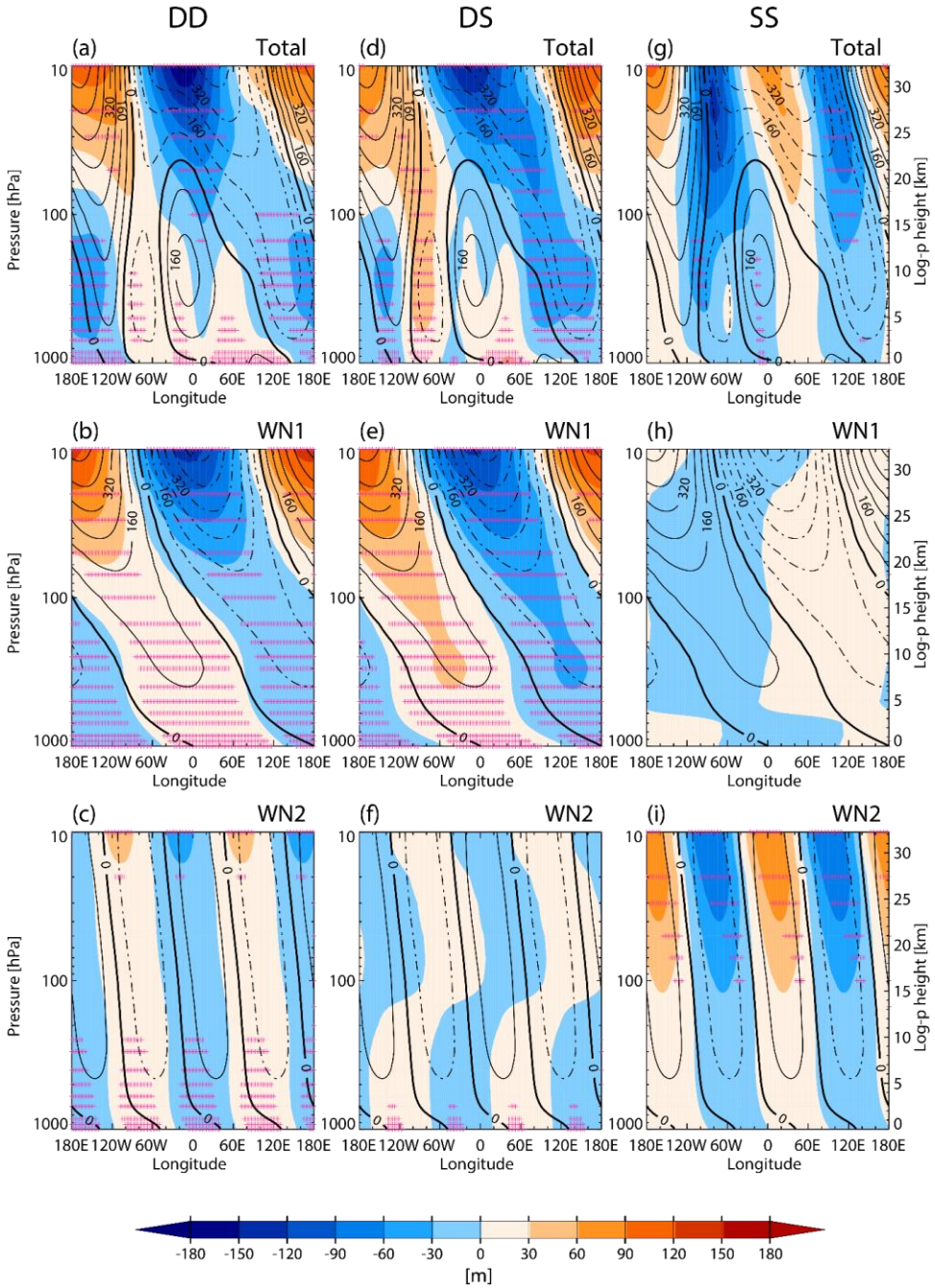

Figure 10. GPH anomaly (shading) and climatological DJF mean values (contours) based on NCEP–NCAR data averaged over days -45 to 0. The GPH is averaged for latitude belts 45°N –75°N. The results are shown for (a)–(c) DD, (d)–(f) DS, and (g)–(i) SS types. From top to bottom, the total

anomaly, wave-1 anomaly, and wave-2 anomaly are given. The bold solid and dashed–dotted contours denote zero and negative values. The contour interval is 80 m. Crosses indicate the statistically significant region at the 90% confidence level.

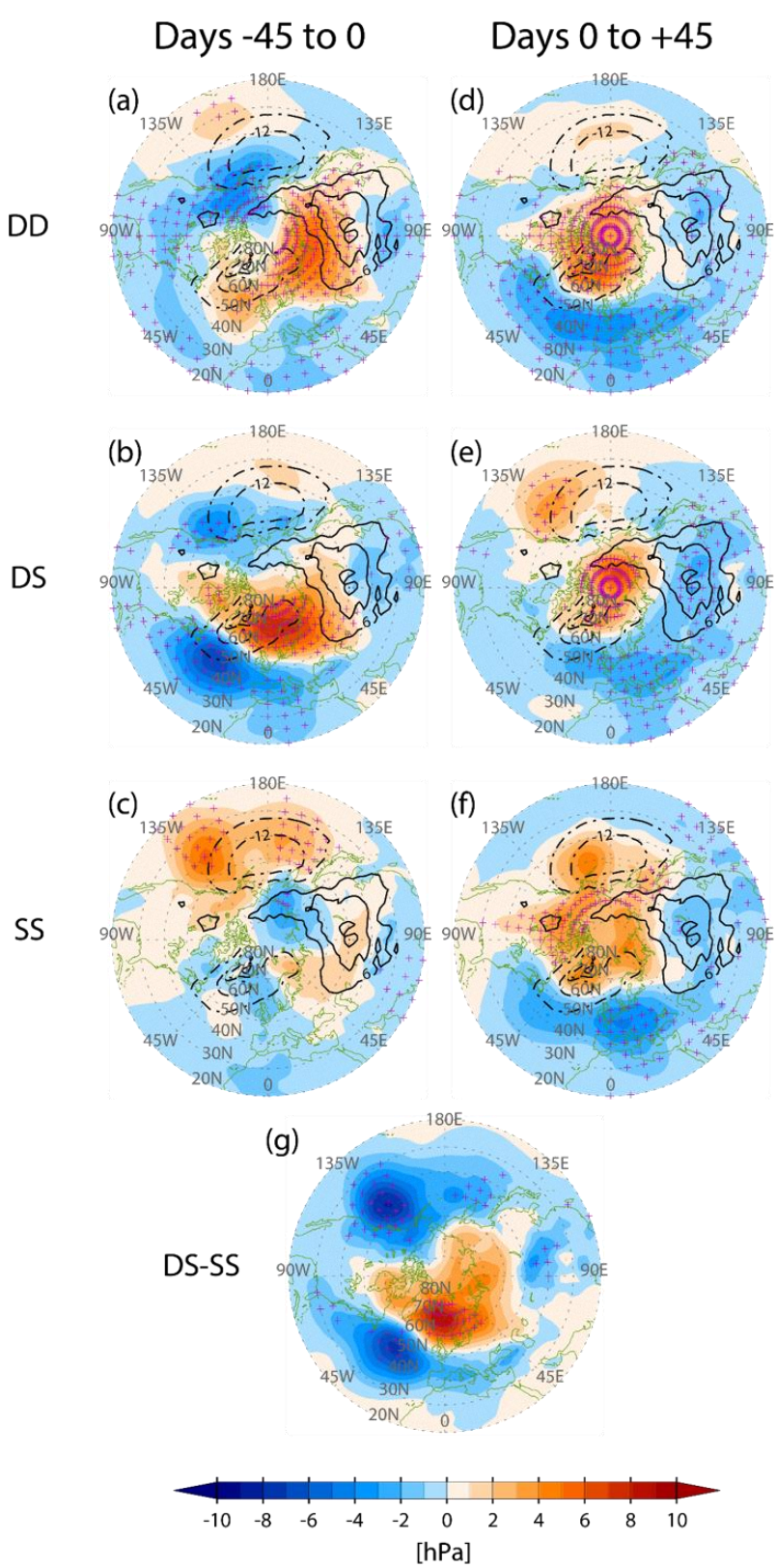
Days -45 to 0
Days 0 to +45
DD
DS
SS
DS-SS
(a)
(b)
(c)
(d)
(e)
(f)
(g)
180E
135W
135E
90W
90E
45W
45E
80N
70N
60N
50N
40N
30N
20N
0
-12
6
-10 -8 -6 -4 -2 0 2 4 6 8 10
[hPa]

Figure 11. (a)-(f) SLP anomaly (shading) and zonal perturbation of DJF mean climatological values (contours) based on NCEP–NCAR data. The left and right panels show features averaged from days -45 to 0, and 0 to +45, respectively. From top to bottom, DD, DS, and SS types are shown. (g) Difference between (b) and (c). The dashed–dotted contour denotes negative values. The contour interval is 6 hPa, and zero contour is omitted. Crosses indicate statistically significant regions at the 90% confidence level.

3.2 Model results

In the model results, SSW events occurred 103 times during the period of analysis. The frequency of SSW events per year, at 0.52, is smaller than that in the MERRA and NCEP–NCAR analyses, at 0.7 and 0.65, respectively. Among the 103 events of simulated SSW, 64 DD types, 31 DS types, and 8 SS types were identified, which implies that displacement-type SSW events were produced twice as often as the split types combining DS and SS in the model. The occurrence of the modeled SS type was about one-fourth that of the DS type, whereas the DS and SS types occurred at comparable rates in the reanalysis data (Table 1). The high and low frequencies of the DD and SS types, respectively, imply that the model is more likely to produce a wave-1 pattern than a wave-2 pattern. Wave-2 amplified SSW is known to be associated with blocking in the Pacific basin region (Martius et al. 2009; Nishii et al. 2011; BC14); however, Pacific blocking was not easily reproduced in the model (De la Torre et al. 2012). Thus, the deficiency in the SS type appears to be consistent with the weak ability of the model in simulating Pacific blocking. The lack of the interannual variability in the boundary conditions of the model could also contribute to the low number of the SS-type SSWs.

The latitude belt selected for calculating the amplitude of the wave component is another factor determining the frequency of each type. We examined the frequencies for the five latitude belts of 10° width, shifting 5° from 45°N–55°N to 65°N–75°N. Table 3 shows the frequency of each SSW type for the five latitude belts according to the model results. These model

frequencies were more sensitive to the selected latitude belt than those of the reanalysis data (Table 2). As the selected latitude belt shifted to lower latitudes, the displacement types decreased, and the split types increased. For example, for the belt of 50°N–60°N, the ratio of displacement type to split type was 1.15, which is similar to that from MERRA, at 1.08. The split-type increase in the model is attributed mostly to the increase in the DS type; the incidence of the SS type was still very low.

To compare the model results with observations, all of the calculations performed by using the reanalysis data were repeated by using the model results. The selected model analyses are shown in Figs. 12 and 14. Fig. 12 shows a time–height cross-section of the composite of the WACCM PCH anomaly for each SSW type. As indicated through a comparison with Fig. 7, the model appeared to effectively reproduce the major characteristic features of the observed SSWs.

The DD type (Fig. 12a) was generally similar to the DS type (Fig. 12b) and the observed DD type (Fig 7a). Beginning on day around –30, positive PCH anomalies for the DD and DS types developed in the upper stratosphere and descended gradually with time. In the SS type from around day -5 sudden positive PCH anomalies were shown along the whole column. After the central day, the simulated DD and DS types showed that the stratospheric positive PCH anomaly descended to the troposphere with time. The negative PCH anomaly in the upper stratosphere also descended to the middle stratosphere. The largest

anomaly appeared in the DS type (Fig. 12b), which agrees with the observations given in Fig. 7b. The model results and observations for the DS type differed, as evidenced by the lack of an ascending positive anomaly in the troposphere 10 days prior to the central day in the model results.

Fig. 12c shows the negative PCH anomaly in the stratosphere from days –35 to –20 and the ascending positive PCH anomaly from the surface from days –10 to 0. The rapid shift in the sign of the PCH anomaly from negative to positive prior to the central day shown in the reanalysis was not clear in the model. The pattern of the ascent near –10 days in the troposphere is similar to that in the observed DS type shown in Fig. 7b.

We compared the composite means of the PCH anomaly from two different latitude belts, 50°N–60°N (Fig. 13) and 55°N–65°N (Fig. 12). In contrast to the frequency change, the composite means of each type did not show significant differences in pattern depending on these two latitude belts.

For comparison with Fig. 8, latitude–altitude cross-sections of the WACCM zonal mean zonal wind anomaly averaged from day –20 to –5 is shown in Fig. 14. Similar to that discussed for Fig. 8, the zonal mean wind patterns in this pre-warming period exhibited relatively large differences among the types. The wind pattern in the DS type in Fig. 14b was more similar to that of the DD type (Fig. 14a) than the SS type (Fig. 14c); this

result was also found in the observed wind fields shown in Fig. 8. In the SS type (Fig. 14c), although the observed wind anomaly in Fig. 8c showed a barotropic dipole pattern throughout the stratosphere, the zonal wind anomaly showed a more complex pattern.

To test if the differences between the three types from WACCM results is statistically significant, the Fig. 15 is drawn. Fig. 15 shows the composite differences of WACCM zonal-mean zonal wind anomaly averaged over day -20 to -5 between three types. As shown in Fig. 14a and 14b, anomalous zonal winds for DD and DS types have similar meridional structures but the intensity is stronger for DD type from the lower to middle stratosphere over the polar region (Fig. 15a). In both Figs. 15b and 15c, similar composite difference patterns are found in polar region: The strong anomalous westerly wind (anomalous easterly wind) in the mid-upper stratosphere (troposphere-lower stratosphere) in the SS type (Fig. 14c) contributes to a negative difference (positive difference). In wide region, these differences are statistically significant as denoted by green crosses and solid circles in Fig. 15, despite large differences in sample size within the types.

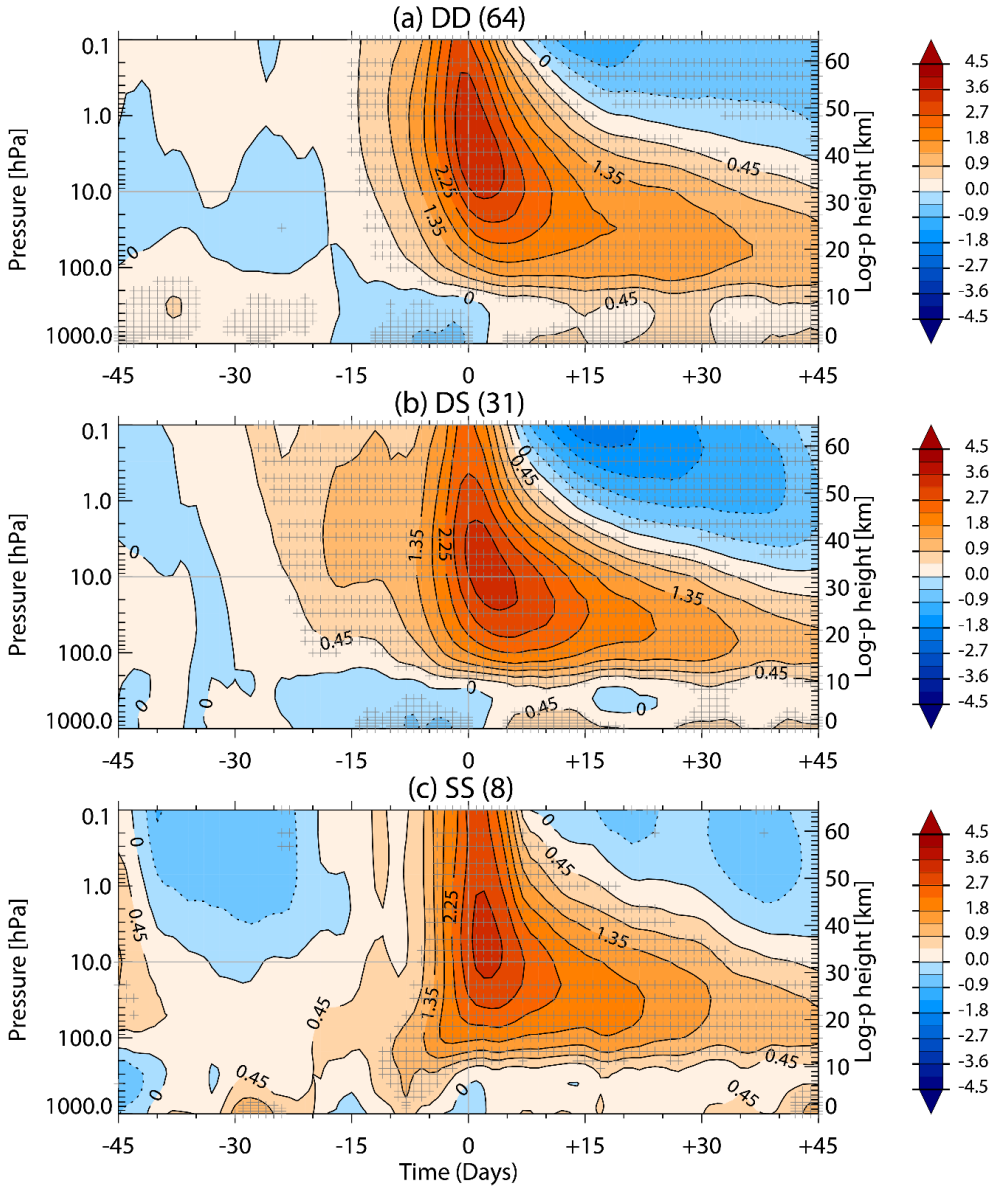

Figure 12. Same as Fig. 7 but for the PCH anomaly calculated by using the WACCM results for (a) 64 DD types, (b) 31 DS types, and (c) 8 SS types.

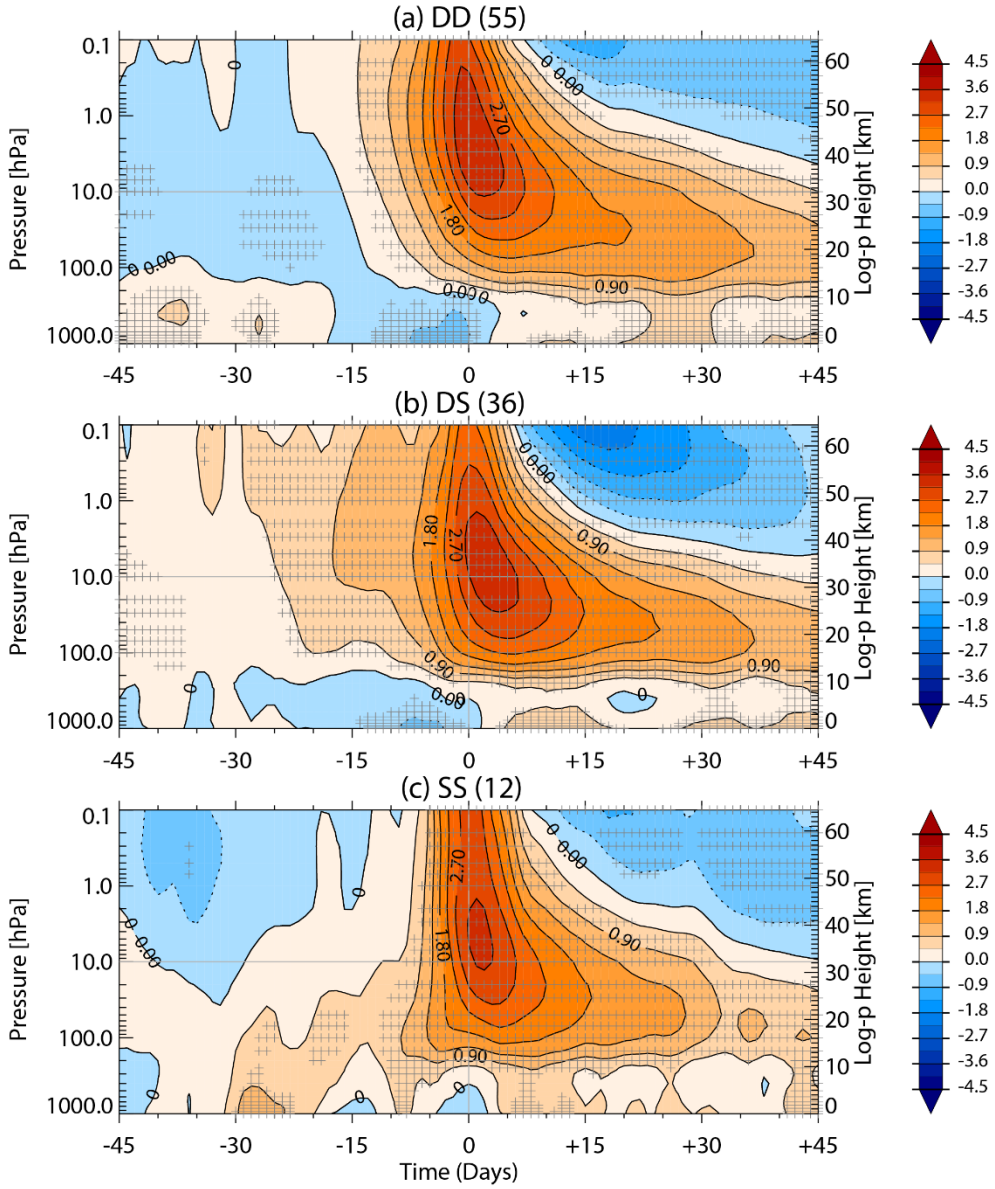

Figure 13. Same as Fig. 7 but for the PCH anomaly calculated by using the WACCM results for (a) 55 DD types, (b) 36 DS types, and (c) 12 SS types. Daily GPH averaged over 50°N-60°N at 10 hPa used for classifying SSW type.

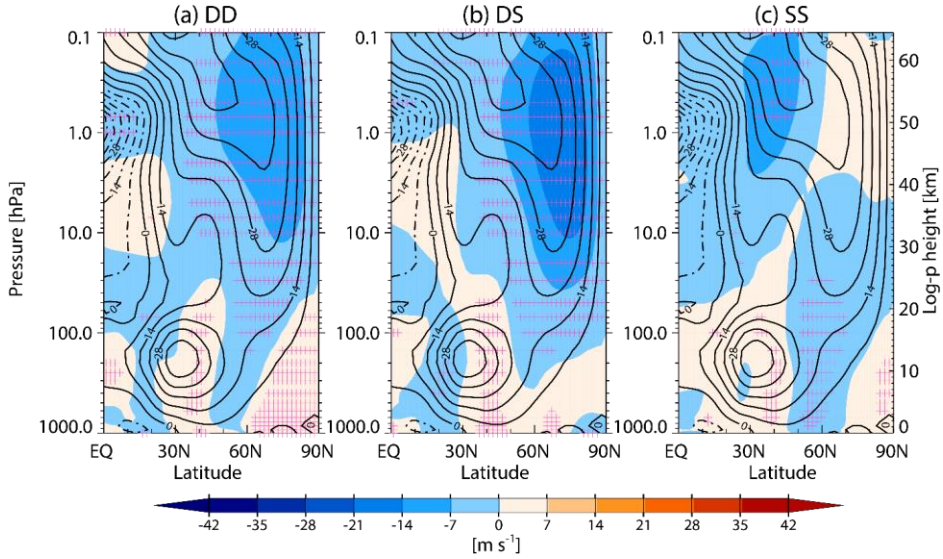

Figure 14. Same as Figs. 8a–c but for WACCM data.

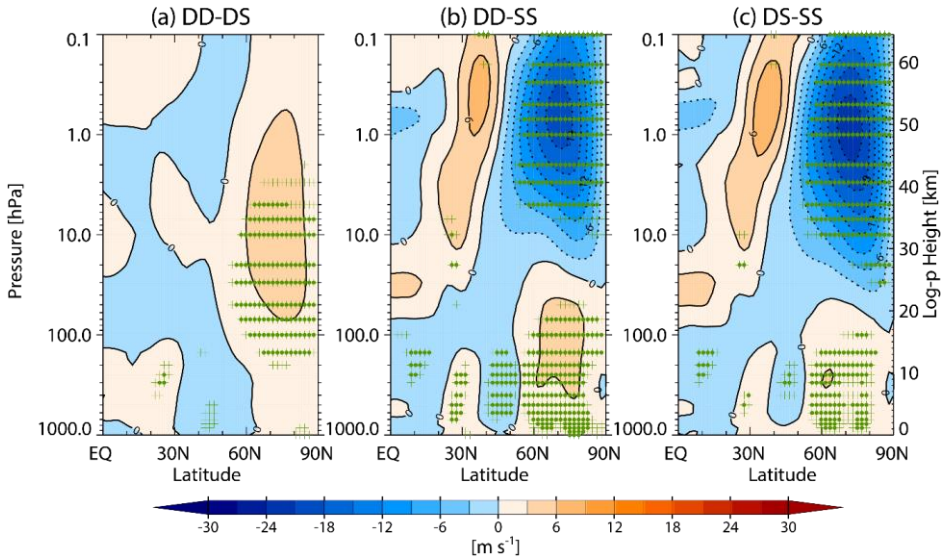

Figure 15. Differences between zonal-mean zonal wind anomalies averaged from day -20 to -5 from WACCM results for (a) DD and DS, (b) DD and SS, and (c) DS and SS. Contour interval is 3 m s^{-1}. Green crosses and solid circles indicate statistically-significant region at 90% and 95% confidence level, respectively. Statistical significance is calculated using the Student's t-test.

Table 3. Same as Table 2 but for WACCM results.

Data	Latitude	Type				Ratio
		DD	DS+SS	DS	SS	DD/(DS+SS)
WACCM	45°N–55°N	40	63	43	20	0.63
	50°N–60°N	55	48	36	12	1.15
	55°N–65°N	**64**	**39**	**31**	**8**	**1.64**
	60°N–70°N	75	28	23	5	2.68
	65°N–75°N	82	21	18	3	3.9

4. Dependence of SSW type-transition on preceding NAO conditions

Although there have been many studies on the classification of SSW types, the factors involved in determining the vortex breaking type remain unknown, especially for DS type. SS type, which is characterized by the presence of two separate vortices before the central day, is distinguishable from DD and DS types and is not related to the NAO phases before the onset. In this section, therefore, we aim to investigate the troposphere precursors by focusing on the North Atlantic for DS-type and DD-type SSWs as will be discussed later.

The predictability of SSW varies with event types (Taguchi, 2018; Domeisen et al., 2019) and dominant wave numbers (Rao et al., 2019). Figure 11 showed that significantly positive sea level pressure anomaly over the Northeast pacific region occurred after the DS-type SSW events whereas the insignificant minor anomaly over that region appeared after DD-type SSW events This suggests the possibility that DD and DS-type SSW events have different effects on tropospheric weather in terms of local scale. Therefore the North Atlantic anomaly responsible for the type transition can provide useful information for prediction of SSW events and tropospheric weather on sub-seasonal to seasonal time scale.

Based on our definition and classification, the numbers of DD- and DS-type events that occurred are 20 and 10 from the NCEP-NCAR reanalysis, 13 and 7 from the MERRA data, and 123 and 55 from the WACCM results, respectively, during the analysis period. These cases were used for a

composite analysis in this study. In both the observation datasets and model, DD- and DS-type events accounted for approximately 50% (60% for the model) and 30% of total SSW cases, respectively.

Both DD and DS types are characterized by displacement of the polar vortex off the pole before the central day. After the occurrence of the SSW, however, one wave form persists in the DD type, whereas for the DS type, the polar vortex splits into two small portions. These two DS-type vortexes are usually located over Eurasia and Canada (not shown).

To identify differences in the mean state between the two types, we calculated composite zonal wind difference (Fig. 16). We find that the zonal wind in the high-latitude lower stratosphere between 100 hPa and 80 hPa is significantly stronger for DD type than for DS type beginning from a month and a half before the occurrence of the SSW. This stronger wind becomes a weaker polar jet in the upper stratosphere beginning from approximately the central day, although this result was statistically insignificant. There are two significant wind difference maxima from the surface to the lower stratosphere near day -40 and day -10. During these periods, zonal wind for DS type weakens significantly from the surface to lower stratosphere (Fig. 17), which can lead to enhancement of the difference in Fig. 16.

To identify any distinctive features in the NAO index between the two types, we plot the temporal evolution of the CPC NAO index smoothed by

a 3-day running mean for the two SSW types as shown in Fig. 18a. Prior to the central day, the negative NAO phase is predominant for the DS type, whereas the positive NAO phase is dominant for the DD type for prolonged periods. The difference in the evolution of the NAO index between DD and DS types is most pronounced between days -49 and -21. For this period, we further examine the relationship between NAO phase and SSW type (Fig. 18b). Based on the CPC NAO index, a positive NAO phase preceded 15 DD-type events out of 20, while a negative NAO phase preceded 9 DS-type events out of 10. However, considering the mean value of the NAO index, the DD-type result is statistically insignificant, whereas the DS-type result is statistically significant. The ESRL/PSD NAO index also indicates a dominantly negative phase before DS-type SSWs, but the relationship between DD-type SSWs and NAO phase is less clear (not shown). This is because a negative NAO phase can also precede the DD-type SSW events. We also conducted the same analysis, shown in Fig. 18, for the SS type. However, the seven SS-type events identified from July 1957 to June 2014 did not have a significant association with a specific NAO phase in the CPC NAO index (not shown).

To examine distinguishable features in the tropospheric pressure pattern between days -49 and -21, we determined the horizontal distributions of the GPH anomaly at 500 hPa (Figs. 19a and 19b). For DD type (Fig. 19a), a positive-NAO like pattern occurs in the North Atlantic region, although it is not significant. A prominent positive height anomaly appears across the Ural Mountains and Siberia, and a significant negative

height anomaly shows over Chukchi and Bering seas. These patterns seem to be similar to wintertime tropospheric wave-1 height (Garfinkel et al., 2010). For DS type (Fig. 19b), on the other hand, the positive height anomaly in the northern part and negative anomaly in the southern part of the North Atlantic resemble the negative NAO pattern, as expected based on Fig. 18. The GPH anomaly at 1000 hPa (Figs. 19c and 19d) also shows similar patterns.

Of the 16 SSW events following the positive NAO phase in Fig. 18b, 15 events are the DD type. This shows that most DD-type SSW events are preceded by positive NAO phase without the type transition. On the other hand, following the negative NAO phase 5 DD types and 9 DS types of SSW events occur. This reveals that SSW events following the negative NAO phase have a strong tendency to change their type.

To determine the influence of anomalous circulation over the North Atlantic region on the vertical structures of planetary waves, we examined the anomalous GPH averaged over days -49 to -21 and days -21 to 0 (Fig. 20). Note that since the contribution of the wave-1 anomaly to the total anomaly before the central day largely outweighs that of the wave-2 anomaly for both types (Fig. 10), we focused on the wave-1 field. From days -49 to -21 (Fig. 20a), the wave-1 anomaly for DD type is tilted eastward with altitude, suppressing the vertical propagation of planetary waves. For DS type (Fig. 20b), on the other hand, planetary waves are tilted westward, which provides favorable conditions for wave propagation. The enhanced

tropospheric ridge over Canada and the North Atlantic (0-120°W) seems to contribute to the development of the ridge in the tropospheric wave-1 anomaly. For DD type, toward the SSW onset from days -21 to 0, on the other hand, positive and negative GPH anomaly fields shift westward with altitude, inducing a constructive structure on the climatological wave fields (Fig. 20c). For DS type (Fig. 20d), an in-phase relationship similar to that of DD type in the anomaly fields occurs but with a smaller amplitude. Notably, the in-phase configuration and upward propagation of planetary waves appear earlier for DS type than for DD type. The difference in vertical structure of planetary wave between the two types shown in Fig. 20 can partially account for the stratospheric wind difference in Fig. 16 because stronger vertical wave propagation slows the jet. The vortex is actually weakened during days -49 to -21. Fig. 21 shows the zonal-mean zonal wind anomaly averaged over days -49 to -21 for DD and DS types. During this period, for DD type, the insignificant positive anomaly is prominent from the troposphere to the stratosphere. On the contrary, for DS type, the polar vortex weakens significantly from the troposphere to the lower stratosphere.

To understand the dependence of SSW type-transition on preceding NAO conditions, we examine the temporal evolution of tropospheric GPH wave-1 and wave-2 anomalies and anomalous meridional eddy heat flux representing the vertical component of the Eliassen-Palm flux for DD and DS types following positive (Fig. 22) and negative (Fig. 23) NAO phases. The NAO phases are determined based on the values averaged over days -

49 to -21 in Fig. 18b. For extratropical climatological wave-1 height, the ridge (purple contour) is located in the North Atlantic and Eurasia, while the trough (green contour) is identified in Siberia and the North Pacific. For extratropical climatological wave-2 height, the ridges are located over Eurasia and the northeast Pacific, while the troughs are found in the Atlantic and over Siberia, respectively.

Regarding the spatio-temporal evolution of tropospheric wave-1 component following the positive NAO phase (Figs. 22a–22d), the ridge over Eurasia and the North Atlantic and the trough over the North Pacific are prominent. This anomalous pattern, in phase with the climatological wave-1 height, can contribute to increase in the magnitude of the climatological wave-1 height. The minor wave-2 anomaly during these periods (Figs. 22e–22h), however, is out of phase with the climatological wave-2 height and leads to decrease in the amplitude of the climatological wave-2 height. The collocation of the anomalous waves can modulate the vertical wave flux (Garfinkel et al., 2010). Figure 22i shows that the wave-1 component in the heat flux anomaly begins to increase by approximately day -21 before the central day. However, the role of the wave-2 component in the heat flux anomaly is marginal throughout the period.

Regarding the spatio-temporal evolution of tropospheric wave-1 component following the negative NAO phase (Figs. 23a–23d), the ridge grows around the northern part of the North Atlantic with time and extends across North America and Eastern Europe, while the trough

develops across Siberia and the Bering Sea. Although the wave-1 anomaly component produced by the North Atlantic anomaly is confined poleward as compared to the climatological wave-1 height, the similarity between the anomalous and climatological stationary wave patterns might lead to an increase in vertical wave flux as shown in Fig. 23i. One noteworthy point is that the wave-2 anomaly (Figs. 23e–23h) is in phase with the climatological wave-2 height, a few days before the central day. This pattern can help enhance wave-2 height and contribute to increase in the vertical wave flux (Fig. 23i), responsible for splitting of stratospheric polar vortex.

We examined the evolution of anomalous meridional eddy heat flux depending on SSW types (Fig. 9). Figures 22i and 23i seem to be similar to the evolution of anomalous meridional eddy heat flux for DD type and DS type, respectively. As discussed above, the evolutions of the tropospheric waves vary, depending on the NAO phase before the central day. The negative NAO phase seems to help develop the wave-2 height before the central day. Therefore, the development of the wave-2 component in the heat flux anomaly prior to the DS-type SSW can be explained by the wave-2 component produced by the North Atlantic anomaly.

Rao et al. (2019) showed that a small scale wave in the troposphere appears a few days before the central day, explaining the elongation and split of the weakened polar vortex for the 2019 mixed-type (displacement to split) SSW based on NCEP-NCAR reanalysis. We do not mean that the preceding NAO phases are the only possible precursors of SSW type

transition. This study will enrich existing literature (Rao et al., 2019) by providing the probability that the North Atlantic anomaly can induce a favorable condition for the development of small scale waves and lead to the occurrence of DS-type SSW.

To improve the confidence level of the observational findings described, we perform numerical experiments using the WACCM model. Similar to the observed results described in Fig. 16, the modeled stratospheric jet in the lower stratosphere prior to DD-type SSWs is significantly stronger than that of the DS type from approximately days -40 to -15 (Fig. 24). The difference in modeled NAO index between DD type and DS type is relatively large between approximately days -35 and -14 rather than days -49 and -21 (Fig. 25a). In other words, the differences in modeled NAO index between the two types are identified as occurring nearer to the central day, while the differences in NAO-related tropospheric patterns are maintained for a shorter period than for the observed results. During this period, approximately two-thirds of all DS-type SSWs correspond to negative NAO phases (Fig. 25b).

The horizontal distributions of simulated 500-hPa GPH anomalies averaged from days -35 to -14 for each type of SSW as shown in Fig 26. For DD type (Fig. 26a), positive anomalies are predominant in the Ural Mountains region and expand to the North Atlantic region, which agrees with the observations. For DS type (Fig. 26b), a negative NAO-like pattern occurs in the North Atlantic region, although it is less prominent than in the

observed results. Notably, we obtained results similar to the observations using a much greater number of SSW events from the simulation, indicating that our results are robust and compelling.

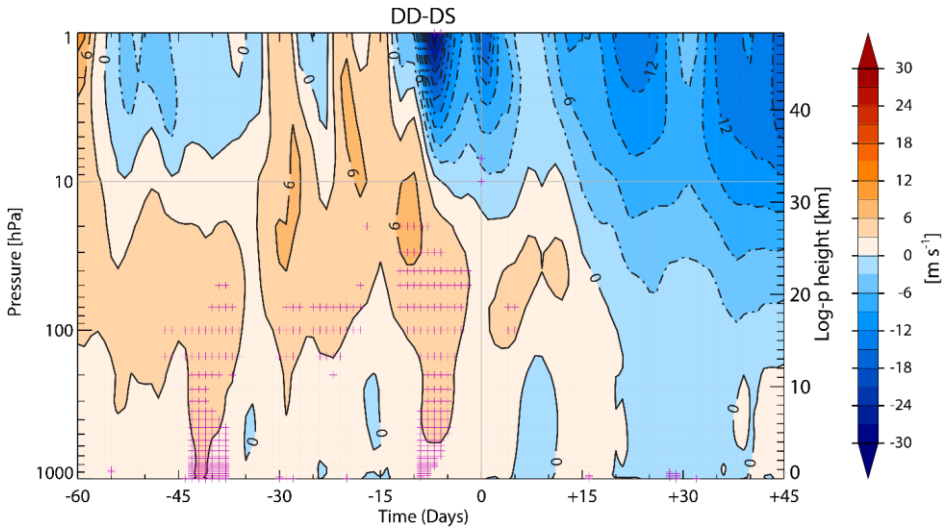

Figure 16. Composite differences of zonal-mean zonal wind averaged over 50°N–70°N between DD and DS events from MERRA (DD minus DS). Gray horizontal and vertical lines denote the 10 hPa level and central day, respectively. The contour interval is 3 m s^{-1}. Pink crosses indicate statistically significant regions at 95% confidence level. Dashed-dotted contours denote negative values.

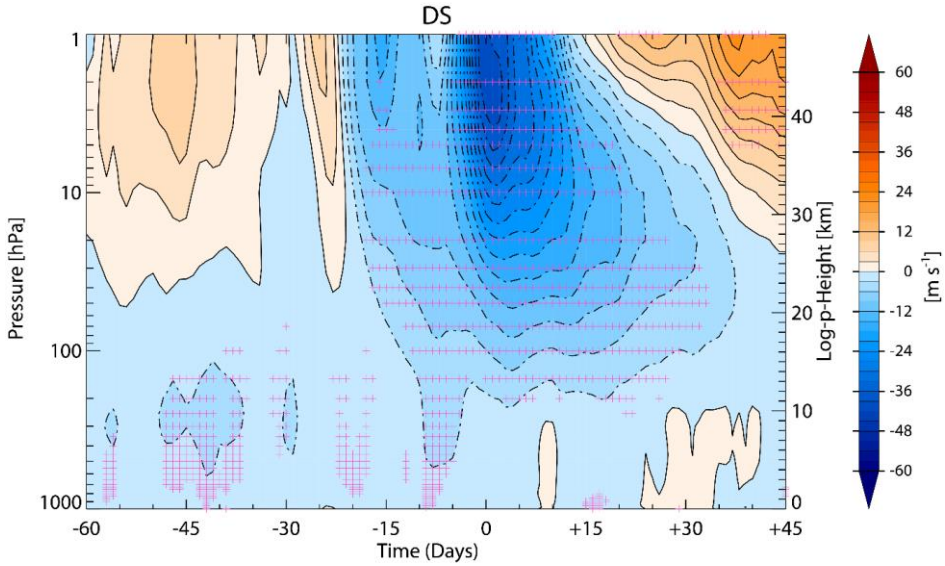

Figure 17. Zonal-mean zonal wind anomaly averaged over 50°N-70°N for DS type from MERRA data. Contour interval is 3 m s^{-1}. Pink crosses indicate statistically significant regions at 95% confidence level. Dashed-dotted contours denote negative values.

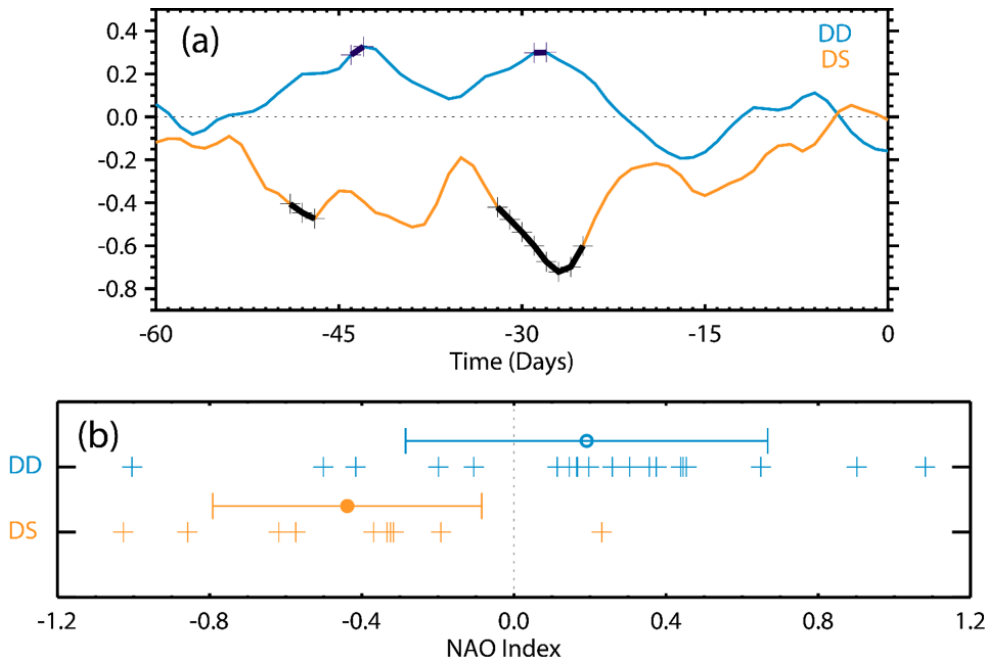

Figure 18. (a) Time series of 3-day running-mean NCEP/CPC NAO index. Blue and orange lines denote DD and DS SSW types, respectively. The bold black solid part of each line with crosses indicates statistically significant periods at 95% confidence level. (b) Scatter plot of CPC NAO index occurring during the two SSW types. The NAO index is averaged over days -49 to -21. The mean NAO index for each type is represented by a closed circle with an error bar indicating one standard deviation. A filled circle denotes a statistically significant value at 95% confidence level.

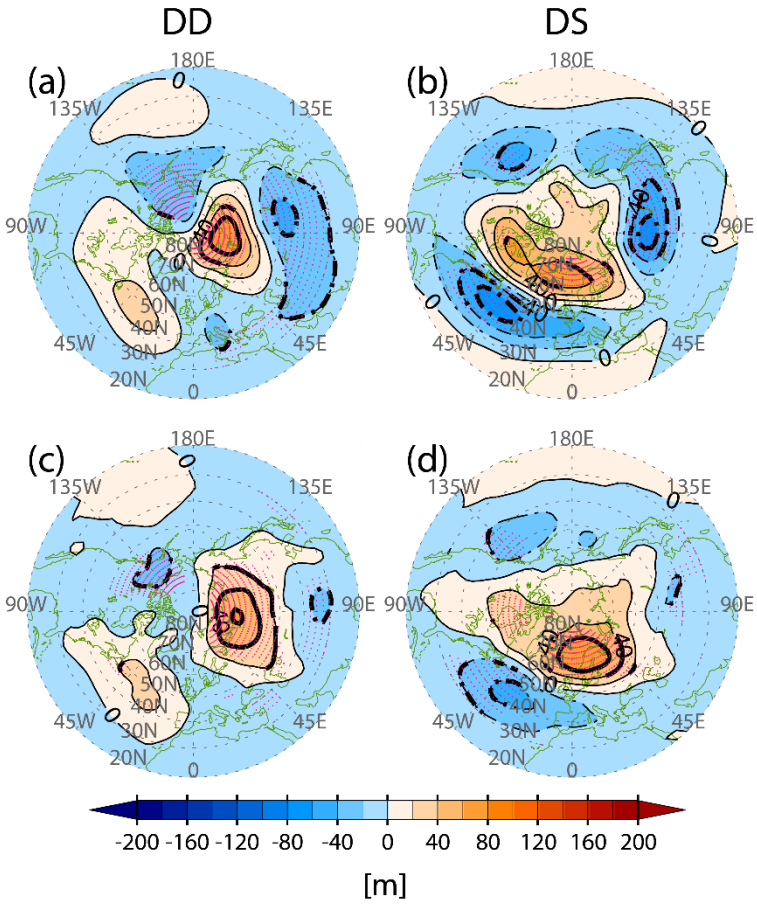

Figure 19. NCEP-NCAR GPH anomalies at 500 hPa averaged over days -49 to -21 for (a) DD and (b) DS types. NCEP-NCAR GPH anomalies at 1000 hPa averaged over days -49 to -21 for (c) DD and (d) DS types. The contour interval is 20 m. Bold contours and pink dots indicate statistically significant regions at 95% confidence level.

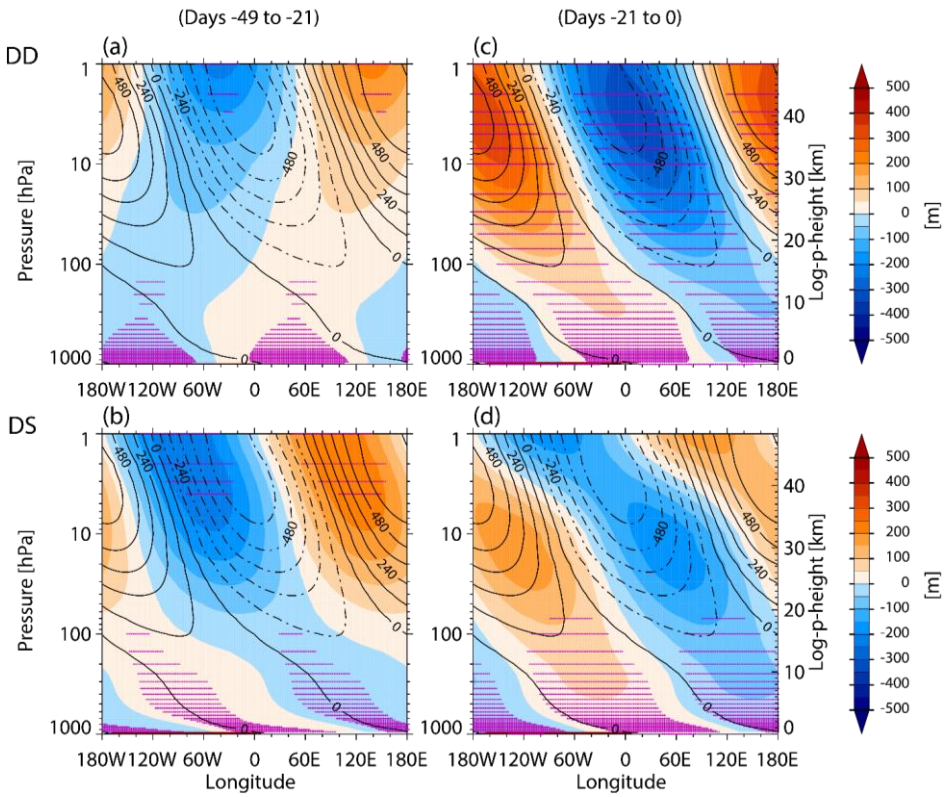

Figure 20. GPH wave-1 anomalies (shading) and climatological DJF-mean value (contour) based on MERRA data averaged over (a) and (b) days -49 to -21 and (c) and (d) days -21 to 0 for (top) DD and (bottom) DS types. The GPH is averaged for latitude belts 45°N–75°N. Solid and dashed-dotted contours denote positive and negative values, respectively. The color intervals are 50 m and contour intervals are 120 m. Pink crosses indicate statistically significant regions at 95% confidence level.

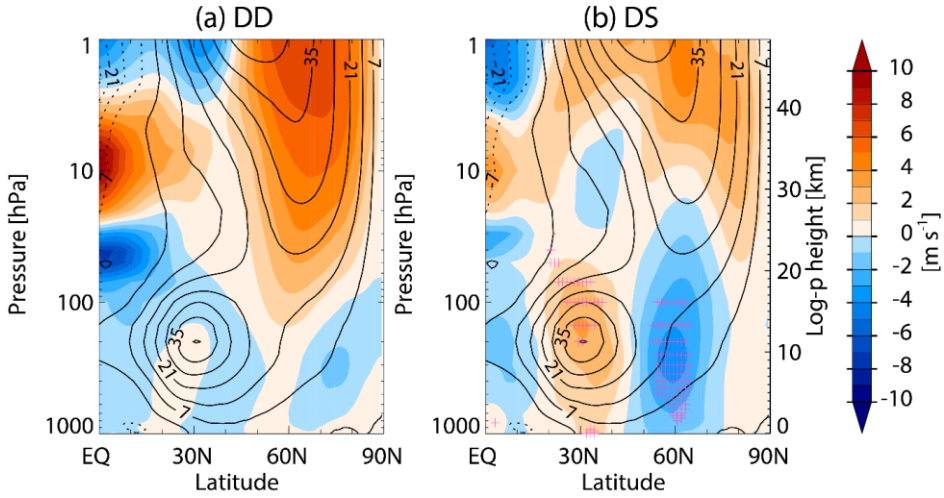

Figure. 21. Zonal-mean zonal wind anomalies (shading) averaged over days -49 to -21 for (a) DD and (b) DS types and climatological DJF mean value (contour) based on MERRA data. Contour interval is 7 m s^{-1}. Crosses indicate the statistically significant region at 95% confidence level.

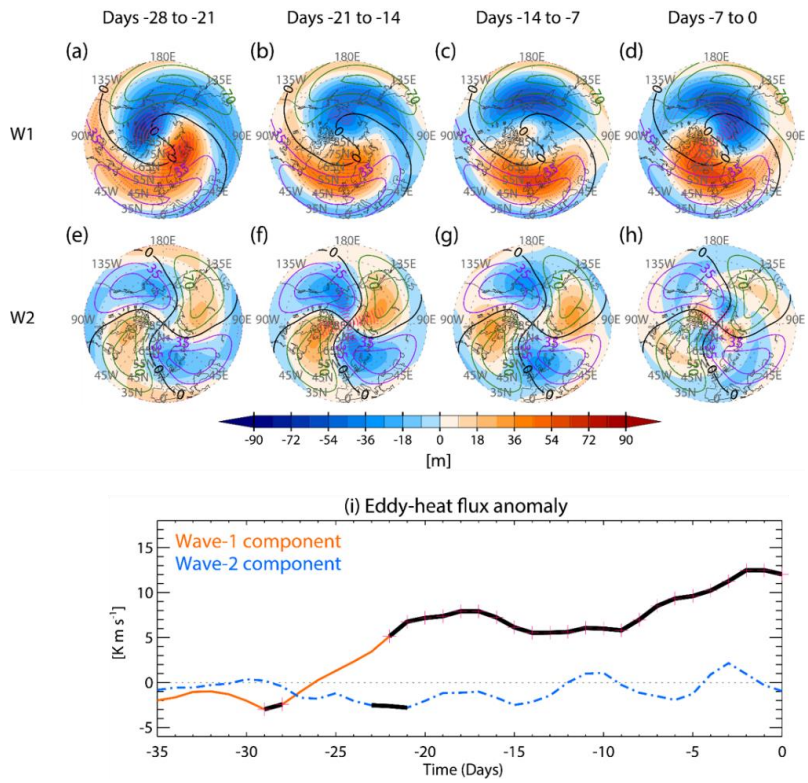

Figure 22. (a)–(h) GPH anomalies at 500 hPa averaged over 7 days from days -28 to 0 for DD and DS types following positive NAO phase and climatological DJF-mean value (contour) based on NCEP-NCAR data. (a)–(d) wave-1 anomaly and (e)–(h) wave-2 anomaly. The color interval is 9 m and contour interval is 35 m. Purple and green contours denote positive and negative values, respectively. The thick solid contour denotes zero value. Pink dots indicate significantly regions at 95% confidence level. (i) Anomalies of meridional eddy heat flux averaged over 45°N–75°N at 100 hPa for DD and DS types following the positive NAO phase based on NCEP-NCAR data. The blue and orange lines denote contributions by zonal waves 1 and 2 to total eddies. Pink crosses and thick solid part of each line indicate significantly regions at 95% and 90% confidence level, respectively.

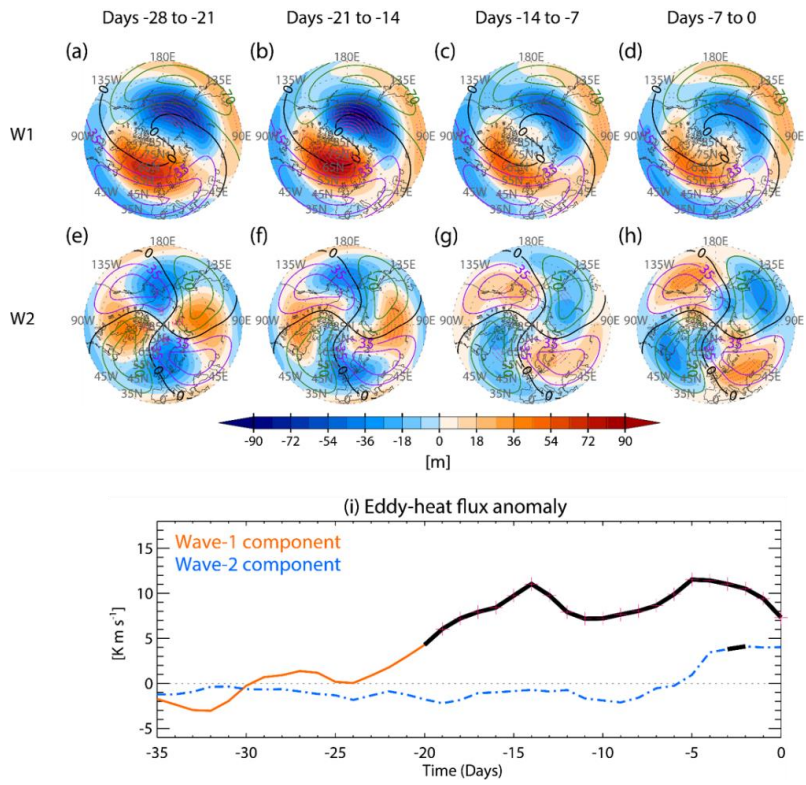

Figure. 23. Same as in Fig. 22 but for negative NAO.

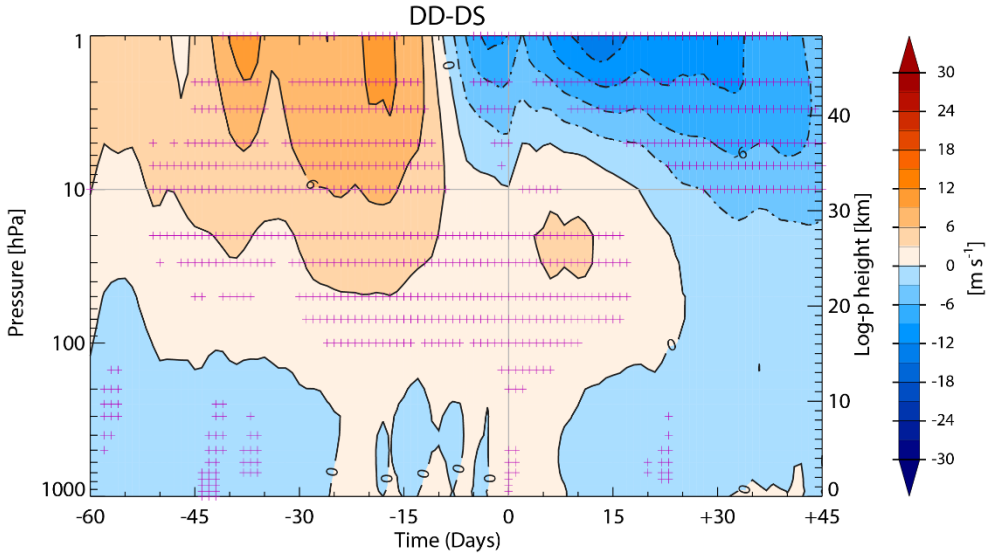

Figure 24. Same as Fig. 16 but for WACCM zonal wind.

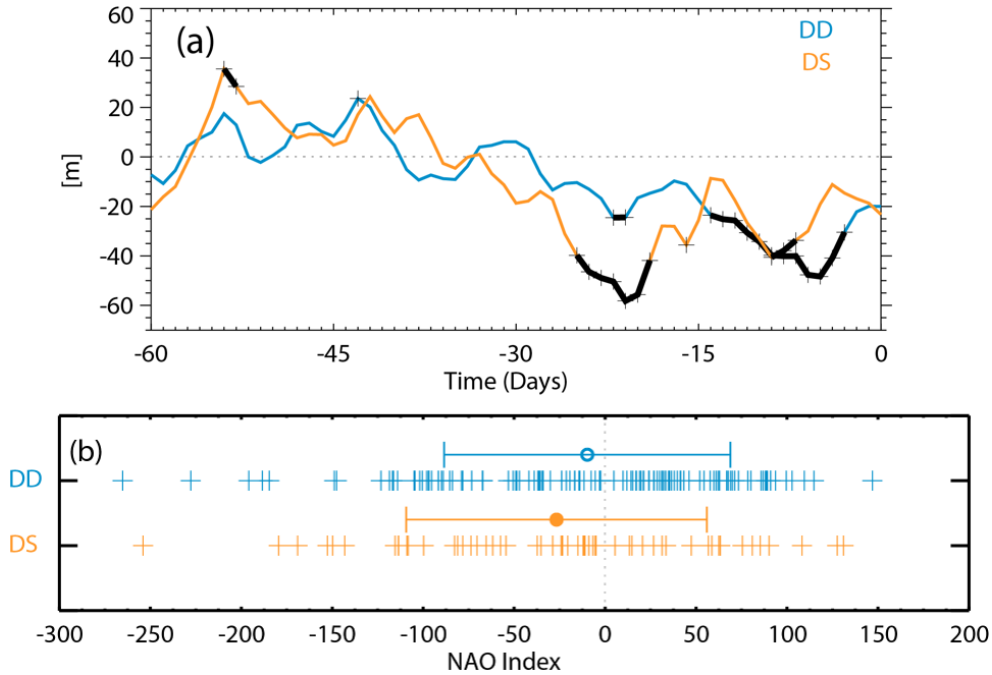

Figure 25. Same as Fig. 18 but for WACCM NAO index.

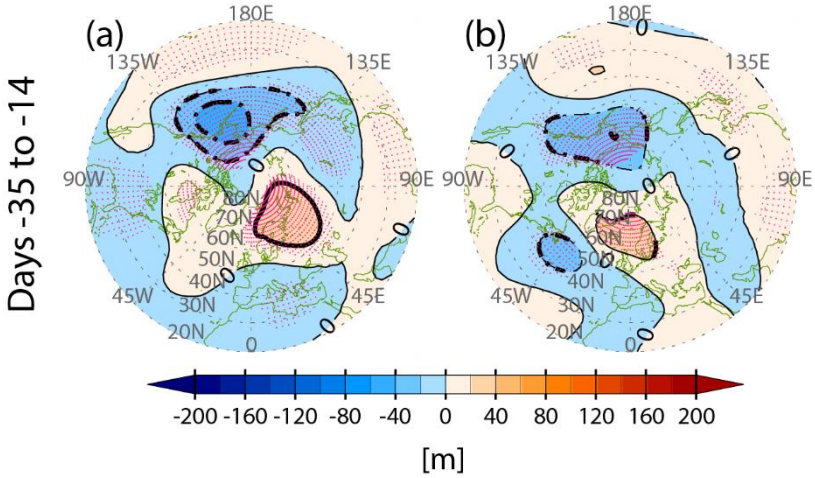

Figure 26. (a) and (b) Same as Figs. 19a and 19b but for WACCM GPH anomalies averaged over days -35 to -14.

5. Summary and future Study

To explain SSW events, major occurrences have been described in previous studies as either displacement or split type according to the shape of the polar vortex. The study by CP07 suggested an objective method of defining the SSW type by using the absolute vorticity on the isobaric surface; their method has been employed in recent studies (Martius et al. 2009; CJ11). Although this method appears to be applicable for separating the two types, it requires complex calculations and specifications of tunable parameters.

In this study, a more simple method was attempted for classifying SSW events by using the wave amplitude of planetary waves because zonal waves 1 and 2 develop during displacement-type and split-type SSW events, respectively. Following the commonly used definition of Butler et al. (2015), the central day of the SSW was specified by reversal of the zonal wind at 60°N and 10 hPa. Classification of the SSW events into two types of wave-1 and wave-2 is easily performed by comparing the wave amplitudes for 21 days from day –10 through day +10, and the results are similar to those reported by CP07 for displacement and split types. Therefore, the classification by wave amplitude performed in this study is at least as reliable as that reported by CP07.

The classification method using daily amplitude has another advantage such that the temporal evolution is clearly revealed before and after the central day. Among the SSW events of the wave-2 type, the first group (Fig.

2a) exhibited the wave-2 shape only after the central day, whereas the second group (Fig. 2b) assumed this shape before and after the central day. Considering the significant differences between these two groups, we separated them into two types, DS and SS. The traditional displacement type is referred to as DD in our notation. The DD and DS types were relatively similar in the pre-warming period.

In the reanalysis data, the incidence number of DS and SS types was similar; however, different characteristics were exhibited including upward-propagating wave activity and a tropospheric height field prior to the central day of the SSW. The DS and SS types exhibited similar wave-2 behavior only close to the central day. Previous studies describing the split type, which is a combination of DS and SS types, appear to preferentially represent the features of the SS type (CP07; CJ11).

We also evaluated the ability of a state-of-art general circulation model in simulating SSW events of different types by using WACCM. In contrast to the classification results obtained by the reanalysis data, in which the DS+SS type occurred almost as often as the DD type, the split type in the WACCM occurred less frequently than the displacement type. Because the split type is simulated mostly in the form of the DS type in the model, and SS-type events are rare, the lower frequency of the split type can be attributed to the lack of SS-type simulations. Therefore, to obtain a more realistic simulation of stratospheric variability using WACCM, further research is needed to understand the reason for the significantly smaller

number of SS events. Both tropospheric wave forcing and stratospheric internal variability of the model should be investigated carefully.

Although the occurrence frequency of the split type in the model tended to be sensitive to the changes in latitude belts used in the classification algorithm, the composite results were similar. The characteristic features reproduced by the model for DD and DS types were similar to those shown in the reanalysis data, whereas the observed and simulated SS types shared fewer similarities.

Although the DD and DS types appear to be similar, the mechanism of the wave 1 change to wave 2 for the DS type remains unknown. In this study, we focus on examining the role of NAO as a precursor for DD- and DS-type SSWs, which account for approximately 80% of total SSW events. The displaced vortex persists for DD type before and after the SSW; however, for DS type, the vortex splits into two after the occurrence of the SSW. We identified significant differences in the strength of the polar stratospheric jet between the two types prior to the SSW event. In the growth stage of SSWs, DS type is characterized by prolonged periods of negative-phase NAO index and tropospheric pressure anomaly fields over the North Atlantic region, which also resemble a negative NAO-like pattern in both reanalysis datasets. The negative NAO phase pattern seems to help develop planetary wave-2 component and consequently leads to splitting of weakening stratospheric vortex. There is a contrasting relationship between DD type and NAO phase to that of DS type. The features of both the DD

and DS types observed in the reanalysis dataset were reproduced well by the model, supporting that the observed results are robust.

In conclusion, atmospheric circulation over the North Atlantic region can induce distinct tropospheric-stratospheric dynamical processes for SSWs and act as a precursor to distinguish SSW events, although the mechanism remains uncertain.

Classifying the SSW events into three types would also help in understanding the relevant dynamics associated with SSW and understanding the North Atlantic variability would help improve predictability for the occurrence of specific types of SSWs. Therefore, this study can contribute to improvement in the predictability of tropospheric weather change because SSW events are known to affect the stratosphere and surface weather (Baldwin and Dunkerton 1999, 2001; Thompson et al. 2002).

References

Albers J. R., and T. Birner, 2014: Vortex preconditioning due to planetary and gravity waves prior to stratospheric sudden warmings. *J. Atmos. Sci.*, **71**, 4028–4054, doi: 10.1175/JAS-D-14-0026.1.

Ambaum, M.H.P. and B.J. Hoskins, 2002: The NAO troposphere–stratosphere connection. *J. Climate*, **15**, 1969–1978. https://doi.org/10.1175/1520-0442(2002)015<1969:TNTSC>2.0.CO;2

Attard, H.E., R. Rios-Berrios, C.T. Guastini, and A.L. Lang, 2016: Tropospheric and stratospheric precursors to the January 2013 sudden stratospheric warming. *Mon. Weather Rev.*, **144**, 1321–1339. https://doi.org/10.1175/MWR-D-15-0175.1.

Ayarzagüena, B., U. Langematz, and E. Serrano, 2011: Tropospheric forcing of the stratosphere: A comparative study of the two different major stratospheric warmings in 2009 and 2010. *J. Geophys. Res.*, **116**, D18114, doi:10.1029/2010JD015023.

Baldwin, M. P., and J. R. Holton, 1988: Climatology of the stratospheric polar vortex and planetary wave breaking. *J. Atmos.Sci.,* **45,** 1123–1142.

Baldwin, M.P., X. Cheng, and T.J. Dunkerton, 1994: Observed correlations between winter-mean tropospheric and stratospheric circulation anomalies. *Geophys. Res. Lett.*, **21**, 1141–1144. https://doi.org/10.1029/94GL01010.

Baldwin, M. P., and T. J. Dunkerton, 1999: Propagation of the Arctic Oscillation from the stratosphere to the troposphere. *J. Geophys.*

Res., **104**, 30937–30946, doi**:**10.1029/1999JD900445.

Baldwin, M. P., and T. J. Dunkerton, 2001: Stratospheric harbingers of anomalous weather regimes. *Science*, **294 (5542)**, 581–584, doi:10.1126/science.1063315.

Bancalá, S., K. Krüger, and M. Giorgetta, 2012: The preconditioning of major sudden stratospheric warmings. *J. Geophys. Res.*, **117**, D04101, doi:10.1029/2011JD016769.

Barriopedro, D., and N. Calvo, 2014: On the relationship between ENSO, stratospheric sudden warmings, and blocking. *J. Climate*, **27**, 4704–4720, doi:10.1175/JCLI-D-13-00770.1.

Butler, A. H., D. J. Seidel, S. C. Hardiman, N. Butchart, T. Birner, and A. Match, 2015: Defining sudden stratospheric warmings. *Bul. Am. Met. Soc*., **96**, 1913–1928.

Charlton, A. J., and L. M. Polvani, 2007: A new look at stratospheric sudden warmings. Part I: Climatology and Modeling Benchmarks. *J. Climate*, **20**, 449-469, doi:10.1175/BAMS-83-11-1631

Cohen, J., and J. Jones, 2011: Tropospheric precursors and stratospheric warmings. J. Climate, 24, 6562–6572, https://doi.org/10.1175/2011JCLI4160.1; Corrigendum, 25, 1779–1790, https://d AU3 oi.org/10.1175/JCLI-D-11-00701.1.

Coy, L., S. Eckermann, K. Hoppel, and F. Sassi, 2011: Mesospheric precursors to the major stratospheric sudden warming of 2009: Validation and dynamical attribution using a ground-to-edge-of-space data assimilation system. *J. Adv. Model. Earth Syst*., **3**, doi:10.1029/2011MS000067.

de la Torre, L., R. R. Garcia, D. Barriopedro, and A. Chandran, 2012: Climatology and characteristics of stratospheric sudden warmings in the Whole Atmosphere Community Climate Model, *J. Geophys. Res.*, **117**, D04110, doi:10.1029/2011JD016840.

Domeisen, D. I. V. and Coauthors, 2019: The role of the stratosphere in subseasonal to seasonal prediction Part I: Predictability of the stratosphere. *Journal of Geophysical Research: Atmospheres*, **124**. https://doi.org/10.1029/2019JD030920.

Garfinkel, C.I., D.L. Hartmann, and F. Sassi, 2010: Tropospheric precursors of anomalous Northern Hemisphere stratospheric polar vortices. *J. Climate*, **23(12)**, 3282-3299. https://doi.org/10.1175/2010JCLI3010.1

Harada, A., A. Goto, H. Hasegawa, N. Fujikawa, H. Naoe, and T. Hirooka, 2010: A major stratospheric sudden warming event in January 2009. *J. Atmos. Sci.*, **67**, 2052–2069, doi: 10.1175/2009JAS3320.1.

Kalnay, E., and Coauthors, 1996: The NCEP/NCAR 40-Year Reanalysis Project. *Bull. Amer. Meteor. Soc.*, **77**, 437–471, doi: 10.1175/15200477(1996)077<0437:TNYRP>2.0.CO;2.

Karpechko, A.Y., A. Charlton-Perez, M. Balmaseda, N. Tyrrell, and F. Vitart, 2018: Predicting sudden stratospheric warming 2018 and its climate impacts with a multimodel ensemble. *Geophys. Res. Lett.*, **24**, 13538–13546. https://doi.org/10.1029/2018GL081091.

Kim, B.-M., S.-W. Son, S.-K. Min, J.-H. Jeong, S.-J. Kim, X. Zhang, T. Shim, and J.-H. Yoon, 2014: Weakening of the stratospheric polar vortex

by Arctic sea-ice loss. *Nat. Commun.*, **5**, 4646, doi:10.1038/ncomms5646.

Kodera, K., B. M. Funatsu, C. Claud, and N. Eguchi, 2015: The role of convective overshooting clouds in tropical stratosphere–troposphere dynamical coupling. *Atmos. Chem. Phys.*, **15**, 6767–6774, doi:10.5194/acp-15-6767-2015.

Kodera, K., H. Mukougawa, P. Maury, M. Ueda, and C. Claud, 2016: Absorbing and reflecting sudden stratospheric warming events and their relationship with tropospheric circulation. *J. Geophys. Res. Atmos.*, **121**, doi:10.1002/2015JD023359.

Kretschmer, M., D. Coumou, L. Agel, M. Barlow, E. Tziperman, and J. Cohen, 2018: More-persistent weak stratospheric polar vortex stateslinked to cold extremes. *Bull. Amer. Meteor. Soc.*, **99(1)**, 49–60. https://doi.org/10.1175/BAMS-D-16-0259.1

Krinitskiy, M., Y. A. Zyulyaeva, and S. K. Gulev, 2019: Clustering of Polar Vortex States Using Convolutional Autoencoders. 52-61. [Available online at http://ceur-ws.org/Vol-2426/paper8.pdf].

Labitzke, K., 1968: Midwinter warmings in the upper stratosphere in 1966. *Quart. J. Roy. Meteor. Soc.*, ***94***, *279-291.* https://doi.org/10.1002/qj.49709440105.

Labitzke, K., 1978: On the different behavior of the zonal harmonic height waves 1 and 2 during the winters 1970/71 and 1971/72. *Mon. Weather Rev.*, **106(12),** 1704–1713. https://doi.org/10.1175/1520-0493(1978)106<1704:OTDBOT>2.0.CO;2.

Lawrence, Z. D., and G. L. Manney 2018: Characterizing stratospheric polar

vortex variability with computer vision techniques. *J. Geophy. Res.,* **121**, 1510–1535. doi.org/10.1002/2017JD027556.

Limpasuvan, V., J. H. Richter, Y. J. Orsolini, F. Stordal, and O.-K. Kvissel, 2011: The roles of planetary and gravity waves during a major stratospheric sudden warming as characterized in WACCM. *J. Atmos. Sol.-Terr. Phys*., **78–79**, 84–98, doi:10.1016/j.jastp.2011.03.004.

Manney, G. L., and Coauthors, 2008: The evolution of the stratopause during the 2006 major warming: Satellite data and assimilated meteorological analyses. *J. Geophys. Res.*, **113**, D11115, doi:10.1029/2007JD009097.

Manney, G. L., M. J. Schwartz, K. Kruger, M. L. Santee, S. Pawson, J. N. Lee, W. H. Daffer, R. A. Fuller, and N. J. Livesey, 2009: Aura Microwave Limb Sounder observations of dynamics and transport during the record-breaking 2009 Arctic stratospheric major warming. *Geophys. Res. Lett.*, **36**, L12815, doi:10.1029/2009GL038586.

Marsh, D. R., M. J. Milis, D. E. Kinnison, J.-F. Lamarque, N. Calvo, and L. M. Polvani, 2013: Climate change from 1850 to 2005 simulated in CESM1 (WACCM). *J. Climate*, **26**, 7372–7391, doi:10.1175/JCLI-D-12-00558.1.

Martius, O., L. M. Polvani, and H. C. Davies, 2009: Blocking precursors to stratospheric sudden warming events. *Geophys. Res. Lett.*, **36**, L14806, doi:10.1029/2009GL038776.

Matsuno, T., 1971: A dynamical model of the stratospheric sudden

warming. *J. Atmos. Sci.*, **28**, 1479–1494. https://doi.org/10.1175/1520-0469(1971)028<1479:ADMOTS>2.0.CO;2.

Matthewman, N. J., J. G. Esler, A. J. Charlton-Perez, and L. M. Polvani, 2009: A new look at stratospheric sudden warmings. Part III: Polar vortex evolution and vertical structure. *J. Climate*, **22**, 1566–1585, doi:10.1175/2008JCLI2365.1.

Mcintyre, M.E., and T.N Palmer, 1983: Breaking planetary waves in the stratosphere, Nature, **305**, 593-594.

Mitchell, D. M., L. J. Gray, J. Anstey, M. P. Baldwin, and A. J. Charlton-Perez, 2013: The Influence of Stratospheric Vortex Displacements and Splits on Surface Climate. *J. Climate*, **26**, 2668–2682, doi:10.1175/JCLI-D-12-00030.1.

Nakagawa, K. I., and K. Yamazaki, 2006: What kind of stratospheric sudden warming propagates to the troposphere? *Geophys. Res. Lett.*, **33,** L04801, doi:10.1029/2005GL024784.

Naujokat, B., K. Kruger, K. Matthes, J. Hoffman, M. Kunze, and K. Labitzke, 2002: The early major warming in December 2001—exceptional? *Geophys. Res. Lett.*, **29**, 2023 http://doi.org/10.1029/2002GL015316.

Neale, R. B., and Coauthors, 2012: Description of the NCAR Community Atmosphere Model (CAM5.0). NCAR/TN-486+STR, 289 pp [Available online at http://www.cesm.ucar.edu/models/cesm1.0/cam/docs/description/cam5_desc.pdf].

Nishii, K., H. Nakamura, and Y. J. Orsolini, 2011: Geographical dependence observed in blocking high influence on the stratospheric variability through enhancement and suppression of upward planetary-wave propagation. *J. Climate*, **24**, 6408–6423, doi:10.1175/JCLI-D-10-05021.1.

O'Neill, A., 2003: Stratospheric sudden warmings. *Encyclopedia of Atmospheric Sciences,* J. R. Holton, J. A. Pyle, and J. A. Curry, Eds., Elsevier, 1342–1353.

Rao, J., C.I. Garfinkel, H. Chen, and I.P. White, 2019: The 2019 New Year stratospheric sudden warming and its real-time predictions in multiple S2Smodels. *Journal of Geophysical Research*, 124. https://doi.org/10.1029/2019JD030826.

Rao, J., R. Ren, H. Chen, X. Liu, Y. Yu, and Y. Yang, 2019: Sub-seasonal to seasonal hindcasts of stratospheric sudden warming by BCC_CSM1.1(m): A comparison with ECMWF. *Adv. Atmos. Sci.*, **36**, 479–494. https://doi.org/10.1007/s00376-018-8165-8.

Rayner, N. A., D. E. Parker, E. B. Horton, C. K. Folland, L. V. Alexander, D. P. Rowell, E. C. Kent, and A. Kaplan, 2003: Global analyses of sea surface temperature, sea ice, and night marine air temperature since the late nineteenth century. *J. Geophys. Res.*, **108**, D14, 4407 doi:10.1029/2002JD002670.

Richter, J. H., F. Sassi, and R. R. Garcia, 2010: Toward a physically based gravity wave source parameterization in a general circulation model. *J. Atmos. Sci.*, **67**, 136–156, doi:10.1175/2009JAS3112.1.

Rienecker, M. M., and Coauthors, 2011: MERRA: NASA's modern-era

retrospective analysis for research and applications. *J. Climate*, **24**, 3624–3648, doi: 10.1175/JCLI-D-11-00015.1.

Smith, K. L., R. R. Neely, D. R. Marsh, and L. M. Polvani, 2014: The specified chemistry whole atmosphere community climate model (SC-WACCM). *J. Adv. Model. Earth Syst.*, **6**, 883–901, doi:10.1002/2014MS000346.

Taguchi, M., 2018: Comparison of subseasonal-to-seasonal model forecasts for major stratospheric sudden warmings. *J. Geophys. Res.*, **123**, 10231–10247. https://doi.org/10.1029/2018jd028755.

Thompson, D. W. J., M. P. Baldwin, and J. M. Wallace, 2002: Stratospheric connection to Northern Hemisphere wintertime weather: Implications for predictions. *J. Climate*, **15**, 1421–1428, doi:10.1175/1520-0442(2002)015<1421:SCTNHW>2.0.CO;2.

Wang, R., Y. Tomikawa, T. Nakamura, K. Huang, S. Zhang, Y. Zhang, H. Yang, and H. Hu, 2016: A mechanism to explain the variations of tropopause and tropopause inversion layer in the Arctic region during a sudden stratospheric warming in 2009. *J. Geophys. Res.*, **121**, 11,932–11,945, doi:10.1002/2016JD024958.

Waugh, D. W., 1997: Elliptical diagnostics of stratospheric polar vortices. *Quart. J. Roy. Meteor. Soc.*, **123,** 1725–1748, doi.org/10.1175/JCLI3996.1

Yoden, S., T. Yamaga, S. Pawson, and U. Langematz, 1999: A composite analysis of the stratospheric sudden warmings simulated in a perpetual January integration of the Berlin TSM GCM. *J. Meteor. Soc. Japan*, **77**, 431–445.

국문초록

성층권 돌연승온의 세 가지 유형 분류

성층권 돌연승온은 극지역 성층권의 대표적인 기상 현상 중 하나로서 북반구 겨울철 극지역 성층권의 온도가 급격히 상승하면서 발생한다. 기존 문헌에서 성층권 돌연승온 현상은 일반적으로 이동 또는 분리 유형으로 정의된다. 이동 유형은 극와도가 극지역에서 벗어나 저위도 방향으로 이동하는 형태이며, 분리 유형은 크기와 강도가 비슷한 두 개의 극와도로 나누어지는 사례이다. 성층권 돌연승온의 발달 과정의 상세한 재검토 결과, 성층권 돌연승온의 일부 사례에서 중심날짜 전후로 그 유형이 변경되는 것으로 밝혀졌다. 관측에서 확인되는 특징을 기반으로, 파동 진폭을 사용하여 세 가지 유형의 성층권 돌연승온, 즉 이동-이동 유형, 이동-분리 유형 및 분리-분리 유형을 객관적으로 정의하였다. 10 hPa 고도의 55°N-65°N 지역에 대해서 평균한 고도장의 동서파수 1 과 2 의 진폭이 분류 기준으로 사용되었다. 동서파수 1 의 진폭이 성층권 돌연승온의 중심날짜 전과 후에 동서파수 2 의 진폭보다 큰 경우, 해당 사례는 이동-이동 유형으로 간주되며, 그 반대의 경우는 분리-분리 유형으로 분류된다. 중심날짜 이전에는 동서파수 1 의 진폭이 동서파수 2 의 진폭보다 크지만 중심날짜 이후에는 더 작은 경우, 해당 성층권 돌연승온 사례는 이동-분리 유형으로 간주된다. 분류 알고리즘은 재분석 자료 및 모델 결과에 각각 적용되었다. 이전 연구들에 의해서 확인된 기존의 분리유형의 성층권 돌연승온 사례들은 이동-분리, 또는 분리-분리 유형으로서 구분 될 수 있고, 각각의 유형은 성층권 돌연승온이 발생 하기 이전에 상대적으로 상이한 특성을 보였다. 분리-분리 유형은 기존의 분리유형의 특징이 보다 명확하며 이동-이동 유형과의 차이가 뚜렷하다. 모델 결과는 전반적으로, 특히 이동-이동 사례에서, 재분석 자료의 분석결과와 유사하다. 또한 성층권 돌연승온 발생과 쇠퇴 시기를 아울러 유형이 전환되는 사례의 발생 여부가 중심날짜 이전에 북대서양 진동의 상태에 기인 할 수 있음을 확인하였다: 양의 북대서양 진동은 대부분 유형의 전환이 없는 이동-이동 유형의 성층권 돌연승온 사례를 선행한다. 반면에 음의 북대서양 진동이 선행하는 경우 성층권 돌연승온 사례들은 유형이 변화하려는 경향성이 강하며 상당수가 이동-분리 유형의 발생으로 이어졌다. 양의 북대서양

진동이 선행되는 조건에서 중심날짜 이전에 연직방향의 파동 활동 대부분이 파수 1 성분에 의해서 설명되며, 이는 음의 북대서양 진동이 선행되는 조건에서 상대적으로 강한 파수 2 성분이 발달하는 것과는 대조된다. 수치실험 결과도 관측자료 분석 결과와 유사하게 확인된다. 따라서 북대서양 진동은 성층권 돌연승온의 유형을 예측하는데 유용한 전구체로 고려 될 수 있다.

주요어 : 성층권 돌연승온, 분류 알고리즘, 이동-이동 유형, 이동-분리 유형, 분리-분리 유형, 북대서양 진동, 전조
학생번호: 2006-30124